1 **First assessment of Aeolus L2A particle backscatter coefficient**

2 **retrievals in the Eastern Mediterranean**

3

4 Antonis Gkikas[1], Anna Gialitaki[1,5,6], Ioannis Binietoglou[1], Eleni Marinou[1], Maria Tsichla[1], Nikolaos

5 Siomos[1], Peristera Paschou[1,5], Anna Kampouri[1,7], Kalliopi Artemis Voudouri[1,5], Emmanouil

6 Proestakis[1], Maria Mylonaki[2], Christina-Anna Papanikolaou[2], Konstantinos Michailidis[5], Holger

7 Baars[3], Anne Grete Straume[4], Dimitris Balis[5], Alexandros Papayannis[2], Tomasso Parrinello[8] and

8 Vassilis Amiridis[1]

9

10 [1]Institute for Astronomy, Astrophysics, Space Applications and Remote Sensing, National Observatory of Athens,

11 Athens, Greece

12 [2]Laser Remote Sensing Unit, Department of Physics, National and Technical University of Athens, Athens, Greece

13 [3]Leibniz-Institut für Troposphärenforschung e.V., Leipzig, Germany

14 [4]European Space Agency (ESA/ESTEC), Noordwijk, Netherlands

15 [5]Laboratory of Atmospheric Physics, Aristotle University of Thessaloniki, Thessaloniki, Greece

16 [6]Department of Physics and Astronomy, University of Leicester, Leicester, United Kingdom

17 [7]Department of Meteorology and Climatology, School of Geology, Aristotle University of Thessaloniki,

18 54124 Thessaloniki, Greece

19 [8]European Space Agency (ESA/ESRIN), Frascati, Italy

20 Corresponding author: Antonis Gkikas (agkikas@noa.gr)

21

22 **Abstract**

23   Since 2018, the Aeolus satellite of the European Space Agency (ESA) acquires wind HLOS

24 (horizontal line-of-sight) profiles throughout the troposphere and up to the lower stratosphere, filling

25 a critical gap of the Global Observing System (GOS). Aeolus, carrying ALADIN, the first UV HSRL

26 Doppler lidar ever placed in space, along with wind HLOS profiles provides also vertically resolved

27 optical properties of particulates (aerosols, hydrometeors). The present study focuses on the

28 assessment of Aeolus L2A particulate backscatter coefficient, retrieved by the Standard Correct

29 Algorithm (SCA), in the Eastern Mediterranean, a region hosting a variety of aerosol species. Ground-

30 based retrievals acquired by lidar instruments operating in Athens (capital of Greece), Thessaloniki

31 (north Greece) and Antikythera (southwest Greece) serve as reference. All lidar stations provide

32 routine measurements to the PANACEA (PANhellenic infrastructure for Atmospheric Composition

33 and climatE chAnge) network. A set of ancillary data including sunphotometric observations

34 (AERONET), reanalysis products (CAMS, MERRA-2), satellite observations (MSG-SEVIRI,

35 MODIS-Aqua) and backward trajectories (FLEXPART) are utilized towards an optimum

Atmospheric
Measurement
Techniques
Discussions

36   characterization of the probed atmospheric conditions under the absence of a classification scheme in

37   Aeolus profiles. First, emphasis is given on the assessment of Aeolus L2A backscatter coefficient

38   under different aerosol scenarios over Antikythera island. Due to the misdetection of the cross-polar

39   component of the backscattered lidar signal, Aeolus underestimates backscatter by up to 33% when

40   non-spherical mineral particles are recorded (10th July 2019). A very good performance is revealed

41   on 3rd July 2019, when homogeneous loads of fine spherical particles are confined below 4 km. The

42   level of agreement between spaceborne and ground-based retrievals varies with altitude when aerosol

43   layers, composed of particles of different origin, are stratified (8th July 2020, 5th August 2020).

44   According to the statistical assessment analysis for 46 identified cases, it is revealed a poor-to-

45   moderate performance for the unfiltered (aerosols plus clouds) Aeolus profiles which improves

46   substantially when cloud contaminated profiles are excluded from the collocated sample. This

47   positive tendency is evident at both Aeolus vertical scales (regular, 24 bins and mid-bin, 23 bins) and

48   it is justified by the drastic reduction of the bias and root-mean-square-error scores. In vertical, Aeolus

49   performance downgrades at the lowermost bins (attributed to either the surface reflectance or the

50   increased noise levels for the Aeolus retrievals and to the overlap issues for the ground-based

51   profiles). Among the three PANACEA stations, the best agreement is found at the remote site of

52   Antikythera with respect to the urban sites of Athens and Thessaloniki. Finally, all key Cal/Val

53   aspects necessary for future relevant studies, the recommendations for a possible Aeolus follow-on

54   mission and an overview of the ongoing related activities are thoroughly discussed.

55

56   **1. Introduction**

57   Atmospheric aerosols constitute a critical component of the Earth system by acting as a major

58   climatic driver (Charlson et al., 1992; Boucher et al., 2013; Li et al., 2022) whereas upon deposition

59   they can affect terrestrial (Okin et al., 2004) and marine ecosystems (Jickells et al., 2005; Li et al.,

60   2018). It is also well documented that they affect several anthropogenic activities with concomitant

61   economic impacts (Middleton et al., 2018; Kosmopoulos et al., 2018). In addition, the accumulation

62   of aerosols at large concentrations causes a degradation of air quality (Kanakidou et al., 2011) with

63   adverse health effects (Pöschl, 2005; Lelieveld et al., 2015) that can increase the mortality rates

64   (Health Effects Institute, 2019; Pye et al., 2021). Therefore, their multifaceted role in

65   multidisciplinary research fields highlights the growing scientific concern in understanding and

66   describing the emission, removal, and transport mechanisms governing airborne particles' life cycle.

67   Due to their pronounced heterogeneity, aerosol burden exhibits a remarkable spatiotemporal

68   variability thus imposing deficiencies in adequately depicting its features and constraints towards a

69   robust assessment of the induced impacts.

70   Passive satellite sensors, providing columnar retrievals of aerosol optical depth (AOD), have

71   been able to reproduce adequately aerosol loads' features across various spatiotemporal scales as it

72   has been justified via the assessment of AOD versus corresponding sun-photometric measurements

73   (e.g., Wei et al., 2019). Nevertheless, the main drawback arises from the sensors' inability to provide

74   information on the vertical distribution of aerosols within the atmosphere. This deficiency hampers a

75   reliable quantification of suspended particles within the planetary boundary layer (PBL), related to

76   health impacts, the three-dimensional reproduction of transported loads in the free troposphere, linked

77   to aerosol-cloud-radiation interactions and associated impacts on atmospheric dynamics (Perez et al.,

78   2006; Gkikas et al., 2018; Haywood et al., 2021), as well as to monitor stratospheric long-lived

79   plumes affecting aerosol-chemistry interactions and perturbing the radiation fields (Solomon et al.,

80   2022). On the contrary, ground-based lidars, relying on active remote sensing techniques, obtain

81   vertical profiles of aerosol optical properties at high vertical and temporal resolution, through multi-

82   wavelength and polarization measurements, as well as the geometric features of the particles' layers.

83   Such observations are performed either at networks distributed across Europe (EARLINET;

84   Papalardo et al., 2014; PollyNET; Baars et al., 2016; Engelmann et al., 2016), United States

85   (MPLNET; Campbell et al., 2002), Asia (AD-NET; Sugimoto et al., 2014) and South America

86   (LALINET; Guerrero-Rascado et al., 2016), or at dedicated experimental campaigns (Ansmann et al.,

87   2011; Weinzierl et al., 2016) or even at open seas (Bohlmann et al., 2018). The reproduction of

88   aerosols' vertical structure at global (Liu et al., 2008) and regional (Marinou et al., 2017; Proestakis

89   et al., 2018) scales has been realized through the utilization of measurements acquired by the Cloud-

90   Aerosol Lidar and Infrared Pathfinder Satellite Observation (CALIOP; Winker et al., 2009) and the

91   Cloud-Aerosol Transport System (CATS; McGill et al., 2015) mounted on the CALIPSO (Cloud-

92   Aerosol Lidar and Infrared Pathfinder Satellite Observation) satellite and the International Space

93   Station (ISS), respectively.

94   On 22nd August 2018, the European Space Agency (ESA) launched its Earth Explorer wind

95   mission, Aeolus. It is the first space-based Doppler Wind lidar worldwide, and was a major step

96   forward for Earth Observations (EO) and atmospheric sciences. The key scientific objective of Aeolus

97   is to improve numerical weather forecasts and to improve our understanding of atmospheric dynamics

98   and their associated impacts on climate (Stoffelen et al., 2005; Isaksen and Rennie, 2019; Rennie and

99   Isaksen, 2019). The first Aeolus wind product assessment, by the Aeolus Data Innovation Science

100   Cluster (DISC) and Cal/Val teams (e.g. Baars, et al., 2020; Lux et al., 2020; Witschas et al., 2020,

101   ESA 2019), during the instrument commissioning phase in autumn 2018 demonstrated that Aeolus

102   could provide physically meaningful winds in near-real-time immediately after the instrument switch-

103   on in September 2018, demonstrating the space-based Doppler wind lidar principle for the first time.

104 However, the analyses also revealed issues with ALADIN's instrument performance and on-ground
105 data processing performance which needed to be mitigated through careful instrument
106 characterization, instrument adjustments, improved data calibration and on-ground data processor
107 updates. After about 1.5 years of instrument and algorithm improvements, the Aeolus L2B wind
108 product was of such good quality that the European Centre for Medium Range Forecasts (ECMWF)
109 could start operational assimilation (January 2020). In May 2020, the L2B wind product could
110 therefore be publicly released, which lead to three further European weather forecast institutes starting
111 operational assimilation of Aeolus winds to Deutsche Wetter Dienst (DWD), Météo-France and the
112 UK MetOffice. All meteorological institutes found that Aeolus winds had significant positive impact
113 on the short and medium term forecasts, with the largest impact in remote areas less covered by other
114 direct wind observations including the tropics, southern hemisphere and polar areas (e.g. ECMWF
115 2020; Rennie et al., 2021).

116 The Aeolus Aladin instrument is a high spectral resolution Doppler wind lidar (HSRL),
117 emitting circularly polarized laser light at 355 nm and observing the co-polarized backscatter from
118 molecules and particles and hydrometeors in two separate channels (Ansmann et al., 2007; Flamant
119 et al., 2008). The backscattered light from the surface or top of optically thick clouds up to 30 km
120 altitude is sampled with a vertical resolution of 24 range bins with a thickness from 250 m up to 2
121 km. The main mission product is profiles of the horizontally projected line-of- sight winds, and spin-
122 off products are the backscatter and extinction coefficient profiles from particles and hydrometeors.
123 In contrast to CALIOP and CATS, ALADIN can retrieve these products without requiring an a priori
124 assumption of the lidar ratio (S), which is characterized by a remarkable variability among aerosol
125 types due to its dependency on particles' shape, composition and size distribution (Müller et al.,
126 2007). However, Aeolus only measures the co-polar part of the atmospheric backscatter and at a
127 single wavelength. Therefore, it is very challenging to discriminate the atmospheric backscatter
128 attributed to aerosols or hydrometeors.

129 A series of errors induced by the instrument, by the retrieval algorithm, or by the type of
130 scatterers probed by Aladin can affect the product quality. It is therefore necessary to perform
131 continuous and extensive calibration and validation (Cal/Val) studies utilizing independent reference
132 measurements (e.g. ground-based, aircraft). This task has been performed by the Aeolus Cal/Val
133 community, responding to the Aeolus Announcement of Opportunity to perform product calibration
134 and validation. Such critical tasks are prerequisites to the acceptance of the Mission as "fit for
135 purpose" as it is underlined in the Aeolus Implementation Cal/Val Plan. In contrast to Aeolus wind
136 retrievals, a very limited number of studies focused on the quality of the L2A optical properties. Abril-

Atmospheric
Measurement
Techniques
Discussions

137   Gago et al. (2022) performed a statistical validation versus ground-based observations from three
138   Iberian ACTRIS/EARLINET lidar stations. Baars et al. (2021) reported an excellent agreement
139   between Aeolus and Polly^{XT} particle backscatter profiles and adequate agreement of extinction and
140   lidar ratio profiles for a case of long range transport of wildfire smoke particles from California to
141   Leipzig (Germany).

142   The current study focuses on the comparison of Aeolus L2A particle backscatter coefficient
143   profiles against ground-based profile observations acquired at three lidar stations (Antikythera,
144   Athens, Thessaloniki) contributing to the Greek National Research Infrastructure (RI) PANACEA,
145   an ACTRIS component, that assures a homogenous quality. All stations are located in the Eastern
146   Mediterranean, a crossroad of air masses (Lelieveld et al., 2002) carrying particles of different nature.
147   The broader Greek area encompasses a variety of aerosol species consisting of: (i) pollutants from
148   industrialized European regions (Gerasopoulos et al., 2003; 2009), (ii) dust aerosols from the nearby
149   deserts (Balis et al., 2004; Papayannis et al., 2005; Gkikas et al., 2016, Marinou et al., 2017), (iii)
150   anthropogenic aerosols from urban areas and megacities (Kanakidou et al., 2011), (iv) biomass
151   burning particles originating in the eastern Europe and the Black Sea (Amiridis et al., 2009; 2010;
152   2012), (v) smoke aerosols subjected to transport at planetary scale (Baars et al., 2019; Gialitaki et al.,
153   2020), (vi) sea-salt particles produced by bursting bubbles during whitecap formation attributed to
154   wind-wave interactions (e.g. Varlas et al., 2021), (vii) biogenic particles such as airborne fungi and
155   pollen grains (e.g. Richardson et al., 2019) and (viii) volcanic ash mixed with sulfate aerosols ejected
156   at high altitudes from explosive Etna eruptions (Zerefos et al., 2006, Kampouri et al., 2021).

157   The manuscript is structured as follows. In Section 2, a brief overview of the Aeolus satellite
158   and the ALADIN instrument is given. The key elements of the Standard Correct Algorithm (SCA)
159   are summarized in Section 3. The technical aspects of the ground-based lidars and the regime of
160   aerosol loads in the surrounding area of the PANACEA stations are presented in Section 4. The
161   collocation criteria between ground-based and spaceborne profiles are described in Section 5. The
162   assessment of Aeolus L2A product under various aerosol scenarios and for the whole collocated
163   sample are discussed in Section 6. The Cal/Val aspects, the recommendations for future relevant
164   studies and the necessary upgrades on ALADIN observational capabilities and Aeolus L2A data
165   content are highlighted in Section 7. Finally, the main findings and the conclusions are drawn in
166   Section 8.

167

168

Atmospheric
Measurement
Techniques
Discussions

Open Access

EGU

2. AEOLUS - ALADIN

A brief description of Aeolus' orbital features, ALADIN's observational geometry and its measurement configuration is given in the current section. This short introduction serves as the starting point for the reader to be familiar with Aeolus' nomenclature. Further details and a more comprehensive overview of the Aeolus satellite mission can be found at ESA technical reports (ESA, 1999; 2008; 2016) and at recently published studies (e.g., Lux et al., 2020; Witschas et al., 2022; Lux et al., 2022).

ESA's Aeolus satellite, named by the 'keeper of winds' according to the Greek mythology (Ingmann and Straume, 2016), flies in a polar sun-synchronous orbit circling the Earth at an altitude of 320 km with a repeat cycle of 7 days (Kanitz et al., 2019a; Straume et al., 2019). The orbital plane forms an angle of 97° with the equatorial plane, the ground track velocity is about 7.2 km/sec and a complete circle around the Earth takes about 90 minutes for each orbit (Lux et al., 2020; Witschas et al., 2020; Straume et al., 2020). Aeolus is flying over the terminator between day and night (dawn/dusk orbit), with its solar panels facing towards the sun direction for minimizing the solar background illumination (Kanitz et al., 2019).

ALADIN, the single payload on the Aeolus satellite platform, is an HSRL lidar (Shipley et al., 1983) equipped with a Nd-YAG laser that emits short laser pulses ($\approx$ 40 to 70 mJ, Witschas et al., 2020) of a circular polarized light at ~355 nm with a 50.5 Hz repetition frequency. The photons that are backscatter from molecules and particulates (aerosols, cloud droplets and ice crystals) at atmospheric altitudes lower than 30 km are captured by a Cassegrain telescope of 1.5 m diameter. The collected photons are directed to the Mie optical channel (Fizeau interferometer) for the analysis of the Doppler shift induced by particulates while the molecular return signals (Rayleigh) are analyzed in two sequentially coupled Fabry–Pérot interferometers (Witschas et al., 2020).

ALADIN provides wind and particulate vertically resolved retrievals along the Line-Of-Sight (LOS) by pointing at a slant angle of 35° off-nadir (see Figure 1 in Flament et al., (2021)) which increases to 37.6°, depending on altitude, due to the curvature of the Earth surface. The instrument detector design allows the sampling of the atmospheric backscatter in 24 vertical bins, with a varying resolution from 0.25 (earth surface) to 2 km (upper atmosphere). The laser pulses are integrated on-board the satellite along the satellite flight direction, to yield measurements of ~3km resolution (integration of ~20 laser pulses). During the on-ground data processing, the measurements are accumulated further to yield an "*observation*" (also called a *Basic Repeat Cycle (BRC)*), which corresponds to a distance of ~90 km. The L2A optical properties product which will be analyzed in the next section, derived by the so-called Standard Correct Algorithm (SCA) (Flament et al., 2021),

202   are provided at the observation scale (on a horizontal resolution of ~90 km) and are available through

203   the Aeolus Online Dissemination System (https://aeolus-ds.eo.esa.int).

204

205   **3. Standard Correct Algorithm (SCA)**

206   Aeolus L2A particulate products are derived by three retrieval algorithms, namely the

207   Standard Correct Algorithm (SCA), the Mie Correct Algorithm (MCA) and the Iterative Correct

208   Algorithm (ICA) and their full description is provided in the Algorithm Theoretical Baseline

209   Document (ATBD; Flamant et al., 2021). MCA relies only on the Mie channel returns and the

210   implementation of the Klett method (Klett, 1981) under the assumption of a universal lidar ratio (~14

211   sr). On the other hand, ICA works under the assumption of different partial filling of the particles

212   within the range bin. Finally, there is also the *group* product in which signals of high signal-to-noise

213   (SNR) ratio are accumulated prior to the implementation of the SCA algorithm. Both ICA and group

214   products are still under development and they are not recommended to be utilized in scientific studies

215   (Flament et al., 2021).

216   Among the aforementioned Aeolus L2A retrieval algorithms, the primary, the most reliable

217   and mature is the SCA. The SCA product is derived from the measured signals on the Mie and

218   Rayleigh channels, which are dependent on the instrument calibration constants (K_{ray}, K_{mie}), the

219   channel cross-talk coefficients C_1, C_2, C_3 and C_4, the laser pulse energy (E_0) and the contributions

220   from the pure molecular (X) and particulate (Y) signals (see Equations 1 and 2 in Flament et al.

221   (2021)). The latter ones, for each bin, result from the vertical integration of the backscatter (either

222   molecular or particulate) where the squared one-way transmission through the atmosphere is taken

223   into account (see Equations 3 and 4 in Flament et al. (2021)).

224   The separation of the molecular and particle signals on each channel is imperfect, due to the

225   HSRL instrument design, which makes necessary a cross-talk correction. The channel cross-talk

226   corresponding to the transmission of the Rayleigh-Brillouin spectrum (depending on the temperature,

227   pressure and the Doppler shift) through the Rayleigh and Mie channels is expressed by the calibration

228   coefficients C_1 and C_4, respectively (Flament et al., 2021). The other two coefficients, C_2 and C_3,

229   refer to the transmission of a Mie spectrum (depending on the Doppler shift) through the Mie and

230   Rayleigh channels, respectively. Along with the "C coefficients", the instrument calibration constants

231   (K_{ray}, K_{mie}) (see in Flament et al., 2021) are included in the AUX_CAL files.

232   Finally, the cross-talk corrected signals, normalized with the range bin thickness and corrected

233   by the range between the satellite and the observed target, are utilized for the retrieval of the vertically

234   resolved backscatter (β) and extinction (α) coefficients. The former, at each bin, is derived by the Y/X

235   ratio multiplied with the molecular backscatter coefficient (see Equations 9 and 10 in Flament et al.,

Atmospheric
Measurement
Techniques
Discussions

Open Access
EGU

236   2021) computed from the pressure and temperature ECMWF simulated fields according to Collis and

237   Russel (1976). For the L2A extinction retrievals, derived via an iterative process from top to bottom,

238   a method called normalized integrated two-way transmission (NITWT) is applied, using measured

239   and simulated pure molecular signals, under the assumption that the particles' extinction at the top-

240   most bin is zero (see equations 11-14 in Flament et al., 2021). This consideration makes the

241   "downwards" solution of the integral equations quite sensitive to the noise within the topmost bin (at

242   altitudes ~20-25 km), which is used as reference for the normalization, particularly under low SNR

243   conditions due to the low molecular density. This is a challenge frequently faced for the Aeolus

244   observations due to the weaker measured signals than those of the pre-launch expectations (Reitebuch

245   et al., 2020) as well as to the possible presence of stratospheric aerosols within the top-most range

246   bin or above. In principle, the extinction is retrieved recursively taking into account the attenuation

247   from the overlying bins and by contrasting observed and simulated molecular signals. By

248   differentiating two consecutive bins, unrealistically high positive or negative extinctions can be

249   retrieved (see Fig. 10 in Flament et al., (2021)) resulting from fluctuations between strong and weak

250   attenuation. In the case of negative extinctions, the SCA algorithm regularizes the solution by

251   resetting extinction to zero (Ehlers et al., 2021), which can lead to an underestimation of the partial

252   column transmission. In order to compensate the impacts of the aforementioned issues, it has been

253   shown by error propagation calculations (see equations 18 and 19 in Flament et al. (2021)), that by

254   averaging two consecutive bins the retrieved extinction becomes more reliable at the expense of the

255   vertical resolution (23 bins; "mid-bin" vertical scale). In contrast to SCA, in the SCA mid-bin

256   negative extinctions can be found since the zero-flooring constraint is not implemented. For

257   consistency reasons, the averaging between two neighboring bins is applied also in the backscatter

258   coefficient thus allowing the derivation of the lidar ratio.

259

4. Ground-based lidars (PANACEA)

261   The ground-based observational datasets used herein, are taken from stations that participate

262   in the PANhellenic infrastructure for Atmospheric Composition and climatE chAnge (PANACEA)

263   initiative. Within PANACEA, adverse measurement techniques and sensors are utilized in a

264   synergistic way for monitoring the atmospheric composition and climate change related parameters

265   in Greece.

266   The locations of the stations providing routine measurements to the PANACEA network are

267   shown in Figure 1-i. For the assessment analysis of Aeolus L2A products, we utilize available

268   measurements from PANACEA stations, namely Antikythera (ANT), Athens (ATH) and

269   Thessaloniki (THE), equipped with multiwavelength polarization lidar systems. All stations comply

Atmospheric
Measurement
Techniques
Discussions

Open Access

EGU

270 with the quality-assurance criteria established within EARLINET (e.g. see Freudenthaler et al., 2016)

271 so as to assure the provision of high-quality aerosol related products. Consequently, the derived

272 datasets can be considered for any validation purpose. To ensure the homogeneity of the optical

273 property profiles derived from the adverse lidar systems operating in each station, the Single Calculus

274 Chain algorithm (SCC; D' Amico et al., 2016; Mattis et al., 2016) was used; an automatic processing

275 chain for lidar data, developed within EARLINET. All systems employ multiple detectors, operating

276 either in the photon-counting or analog mode. Herein elastically and inelastically backscattered

277 signals at 355 and 387 nm, were used to evaluate Aeolus products. The optical property profiles were

278 derived using the Raman and Klett-Fernald-Sassano inversion methods (Ansmann et al. 1992;

279 Fernald, 1984; Klett, 1981; Sasano and Nakame, 1984) during night-time and daytime measurements

280 respectively. Below the full overlap height and under the assumption of a well-mixed boundary layer,

281 lidar profiles can be linearly extended to the ground (Siomos et al., 2018, Baars et al., 2016).

282

283 *4.1 Antikythera*

284 Regular lidar measurements have been performed at the PANGEA observatory (PANhellenic

285 GEophysical observatory of Antikythera; lat=35.86 N, lon=23.31 E, alt=193 m asl.) contributing to

286 this study. Under the prevailing Mediterranean background conditions, and being across the traveled

287 path of different air masses (i.e. marine particles, Saharan dust), Antikythera is considered as an ideal

288 location for Cal/Val activities.

289 The lidar system deployed at PANGEA is operated by the National Observatory of Athens

290 (NOA). It is a Polly[XT] (Engelmann et al., 2016) multi-wavelength Polarization-Raman-Water vapor

291 lidar, designed for unattended, continuous operation. Polly[XT] deploys an Nd:YAG laser which emits

292 linearly polarized light at 355, 532 and 1064 nm. The radiation elastically and inelastically

293 backscattered from aerosol, cloud particles, nitrogen (at 387 and 607 nm) and water vapor (at 407

294 nm) molecules, is collected using a near-range (spherical mirror of 50 mm diameter, focal length

295 f=250 mm and 2.2 mrad field of view (FOV)) and a far-range receiver (Newtonian telescope with a

296 300 mm diameter primary mirror, f=900 m and 1 mrad FOV) at a raw vertical resolution of 7.5m.

297 The combined use of the near-range and far-range receivers allows for the retrieval of the aerosol

298 optical properties from 500 m up to ~12-14 km above the ground. A detailed description of the

299 technical characteristics of Polly[XT] can be found in Engelmann et al. (2016).

300

301 *4.2 Athens*

302 The Laser Remote Sensing Unit of the National and Technical University of Athens, Greece

303 (LRSU; NTUA; lat=37.96 N, lon=23.78 E, alt=200 m asl.), is part of the EARLINET since May

304   2000. Currently, the Athens lidar station performs simultaneous measurements with two different

305   lidar systems, EOLE and DEPOLE. The EOLE lidar is an advanced 6-wavelength elastic

306   backscatter/Raman lidar system able to provide the aerosol backscatter coefficient at 355, 532 and

307   1064 nm, the aerosol extinction coefficient at 354 and 532 nm and water vapor mixing ratio profiles

308   in the troposphere. EOLE is based on a pulsed Nd:YAG laser system and a 300 mm diameter

309   Cassegrain telescope (f=600 mm, FOV =1.5 mrad) which collects all elastically backscattered lidar

310   signals (355-532-1064 nm), as well as those generated by the spontaneous Raman effect (by

311   atmospheric N_2 at 387-607 nm and by H_2O at 407 nm). The full overlap (i.e. the altitude from which

312   upwards the whole lidar beam is within the telescope FOV) of EOLE is reached at, approximately,

313   812 m a.s.l..

314   The DEPOLE lidar is a depolarization lidar, able to provide profiles of the aerosol backscatter

315   coefficient and the linear particle/volume depolarization ratio at 355 nm. DEPOLE is based on a

316   pulsed Nd:YAG laser system which emits linearly polarized light at 355 nm. The elastically

317   backscattered lidar signal at 355 nm is collected by a 200 m diameter Dall-Kirkham/Cassegrain

318   telescope (f=600 mm, FOV=3.13 mrad) and the full overlap is reached at, approximately, 500 m a.s.l..

319

320   *4.3 Thessaloniki*

321   Thessaloniki's multiwavelength Polarization Raman lidar system (THELISYS) belongs to the

322   Laboratory of Atmospheric Physics that is located in the Physics Department of the Aristotle

323   University of Thessaloniki (lat = 40.63 N, lon = 22.96 E, a.s.l. = 50m). Thessaloniki is a member

324   station of the EARLINET since 2000, providing almost continuous measurements, according to the

325   network schedule (every Monday morning, ideally close to 12:00 UTC, and every Monday and

326   Thursday evening) and during extreme events (e.g., Saharan dust outbreaks, smoke transport from

327   biomass burning, volcanic eruptions) and satellite overpasses. THELISYS has been validated within

328   EARLINET at hardware level by two intercomparison campaigns (Matthias et al., 2004), in order to

329   fulfill the standardized criteria. The system is based on the first (1064 nm), second (532 nm), and

330   third harmonic (355 nm) frequency of a compact, pulsed Nd:YAG laser emitted with a 10 Hz

331   repetition rate. THELISIS setup includes three elastic backscatter channels at 355, 532 and 1064nm,

332   two nitrogen Raman channels at 387 nm and 607nm, and two polarization sensitive channels at 532

333   nm. The acquisition system is based on a LICEL Transient Digitizer working in both the analogue

334   and photon counting (250 MHz) mode. The vertical resolution of the elastic raw signal at 355 nm is

335   equal to 3.75 m and is recorded in both analog and photon counting mode. The full overlap height is

336   almost 800m a.s.l. A detailed description of THELISIS can be found in Siomos et al. (2018) and

337   Voudouri et al. (2020).

338   *4.4. Aerosols' load variability in the vicinity of the PANACEA sites*

339   The variability of the atmospheric aerosol load in the vicinity of three PANACEA stations

340   (Fig. 1-i) is discussed in this section. The aim of this introductory analysis is to investigate the

341   horizontal homogeneity of the aerosol optical depth (AOD) in the respective broader areas, playing a

342   key role in the comparison of ground-based and spaceborne profiles, which are not spatially

343   coincident as it will be shown in a following section (i.e., collocation method). For the purposes of

344   this analysis, we have processed the mid-visible (550 nm) AOD retrievals, over the period 2008-2017,

345   acquired by the MODIS sensor, mounted on the Aqua polar orbiting satellite. More specifically, we

346   have analyzed the Level 2 (L2) MODIS-Aqua AODs, obtained by the latest version (Collection 6.1)

347   of the operational retrieval algorithms (Remer et al., 2008; Levy et al., 2013; Sayer et al., 2013),

348   accessible from the Level 1 and Atmosphere Archive and Distribution System (LAADS) Distributed

349   Active Archive Center (DAAC) (https://ladsweb.modaps.eosdis.nasa.gov/, last access: 17 June

350   2022).

351   For each station, we have calculated the average AOD values within progressively larger

352   circular areas, with radii spanning from 10 to 100 km with an incremental step of 10 km (Fig. 1-ii).

353   Figure 1-iii illustrates the resulting AODs for each station (x labels) and at each radius (colored bars).

354   In order to ensure the reliability of the obtained results, only the best (QA=3) MODIS-Aqua AOD L2

355   retrievals are considered whereas the spatial averages are calculated only when the satellite

356   observations are simultaneously available at all circles. In the urban areas of Athens (ATH) and

357   Thessaloniki (THE), the contribution of anthropogenic aerosols on the columnar load fades for

358   increasing radii. On the contrary, at Antikythera (ANT), the spatial AOD means remain almost

359   constant revealing a horizontal homogeneity of the aerosol load in the broader area. An alternative

360   way to compare the differences in the AOD spatial representativeness between the urban (ATH, THE)

361   and the remote (ANT) sites is depicted in Fig. 1-iv showing the normalized values for each radius

362   with respect to the AOD levels of the inner circle (i.e., up to 10 km distance from the station). In both

363   urban sites the values are lower than one (dashed line), decreasing steadily in THE and smoothly in

364   ATH after an abrupt reduction from 10 to 20 km. In ANT, the blue curve resides almost on top of the

365   dashed line, throughout the circles radii (i.e., range of distances) indicating the absence of significant

366   horizontal variation of the aerosol load suspended in the surrounding area of the station.

367

368   **5. Collocation between Aeolus and ground-based lidars**

369   The assessment of Aeolus L2A backscatter profiles has been performed against the

370   corresponding measurements acquired at the three EARLINET/PANACEA lidar stations. In Figure

371   2, three examples of the collocation between ground-based and spaceborne retrievals are illustrated

372 in order to describe our approach as well as to clarify points needed in the discussion of the evaluation

373 results (Section 6). At each station, we identify the observations (BRCs), considering their

374 coordinates at the beginning of the ALADIN scan, falling within a circle of 120 km radius (black

375 dashed circle) centered at the station coordinates (black dot). Based on the defined spatial criterion,

376 the number of BRCs residing within the 120 km circle should be at least one and cannot be more than

377 three. We denote each one of them, along the ALADIN measurement track (white stripe), with

378 different colors (red, blue and magenta) in Fig. 2. The orange arrow shows the flight direction of the

379 satellite for the dusk (ascending) or dawn (descending) orbits. For the ground-based observations, the

380 aerosol backscatter profiles are derived considering a time window of ± 1 hour around the satellite

381 overpass. Nevertheless, this temporal collocation criterion has been relaxed or shifted in few cases to

382 improve the quality of the ground-based retrievals as well as to increase the matched pairs with Aeolus

383 L2A profiles. Overall, 46 cases are analyzed out of which 15 have been identified over Antikythera,

384 12 in Athens and the rest 16 in Thessaloniki.

385   The ground-based profiles are derived under cloud free conditions in contrast to Aeolus L2A

386 backscatter profiles providing aerosol and/or cloud backscatter. Therefore, a cloud screening of the

387 Aeolus data using auxiliary cloud information was applied. In the framework of the present study, the

388 exclusion of cloud contaminated Aeolus profiles relies on the joint processing of the cloud mask

389 product (CLM; https://www.eumetsat.int/media/38993) derived by radiances acquired by the SEVIRI

390 (Spinning Enhanced Visible and Infrared Imager) instrument mounted on the Meteosat Second

391 Generation (MSG4) geostationary satellite (Schmetz et al., 2002). It should be noted, however, that

392 the CLM product serves as an indication of clouds presence, without providing information about

393 their macrophysical properties (i.e., cloud coverage), their phase (i.e., ice, water, mixed) or their

394 categories (i.e., low, middle, high). In the illustration examples of Figure 2, the grey shaded areas

395 represent the spatial coverage of CLM in the broader area at each PANACEA site. Based on the

396 filtering procedures, the Aeolus L2A backscatter retrievals, throughout the probed atmosphere by

397 ALADIN, are removed from the analysis when the grey shaded areas overlap with a BRC.

398
399 **6. Results**

400 *6.1 Assessment of Aeolus L2A backscatter under different aerosol scenarios*

401   In the first part of the analysis we assess the quality of the Aeolus L2A backscatter under

402 various aerosol regimes aiming to: (i) investigate the capabilities of the ALADIN spaceborne lidar to

403 detect aerosol layers, (ii) investigate how the horizontal homogeneity and vertical structure of the

404 aerosol layers can affect the level of agreement between spaceborne and ground-based retrievals and

405 (iii) demonstrate the synergistic use of various datasets for a better characterization of the prevailing

406   aerosol conditions. All of these aspects are necessary towards a comprehensive Cal/Val study for

407   facilitating the interpretation of the obtained findings and at a further step for identifying possible

408   upgrades on Aeolus retrievals. Overall, four cases over the Antikythera island (southwest Greece) are

409   analyzed for the Aeolus L2A aerosol backscatter retrievals (Baseline 2A11) and the obtained results

410   are depicted in Figure 3.

411   As it has been already mentioned, Aeolus retrievals are representative at coarse spatial (BRC

412   level; ~90 km) and vertical (minimum 250 m) resolution, while currently there is no scene

413   classification scheme. In order to overcome this inherent limitation, as much as possible, several

414   ancillary data and products are utilized in parallel with those of the MSG-SEVIRI CLM product.

415   Based on the FLEXPART v10.4 Lagrangian transport model (Stohl et al., 2005; Ignacio Pisso et al.,

416   2019) we have reproduced the 5-day air masses backtrajectories prior to their arrival at 7 altitudes

417   above the ground station. FLEXPART was driven with 3-hourly meteorological data from the

418   National Centers for Environmental Prediction (NCEP) Global Forecast System (GFS) analyses

419   provided at $0.5° \times 0.5°$ resolution and for 41 model sigma pressure levels

420   (https://nomads.ncep.noaa.gov/txt_descriptions/GFS_half_degree_doc.shtml). For depicting the

421   spatial patterns of the mid-visible (550 nm) total and speciated AOD, we are relying on the MERRA-

422   2 (Modern-Era Retrospective analysis for Research and Applications version 2; Buchard et al., 2017;

423   Randles et al., 2017; Gelaro et al., 2017) and CAMS (Copernicus Atmosphere Monitoring Service;

424   Inness et al., 2019) reanalysis datasets, both providing aerosol products of high quality (Gueymard

425   and Yang, 2020; Errera et al., 2021). Finally, AERONET sun-direct measurements (Level 1.5,

426   Version 3; Giles et al., 2019; Sinyuk et al., 2020) of spectral AODs and Ångström exponent are also

427   used for the characterization and the temporal evolution of the aerosol load over the station.

428

429   *6.1.1 Dust advection on 10th of July 2019*

430   The first case refers to the advection of dust aerosols from northwest Africa towards the

431   Antikythera island with dust-laden air masses crossing southern Italy prior to their arrival to the

432   PANACEA site from northwest directions (Figure S4). This route of air masses, driven by the

433   prevailing atmospheric circulation (Gkikas et al., 2015), is typical during summer when Saharan

434   aerosols are advected towards the eastern Mediterranean (Balis et al., 2006). MERRA-2 (Fig. S3-i)

435   and CAMS (Fig. S3-ii) show a reduction of AODs from west to east whereas the large contribution

436   (>80%) of dust aerosols to the total aerosol load is evident in both reanalysis products (results not

437   shown here). The moderate-to-high AOD values are confirmed by the ground-based sunphotometric

438   measurements (Fig. S1) and are associated with low Ångström exponent values (0.2 – 0.4) thus

439   indicating the prevalence of coarse particles. This is further supported from Polly[XT] measurements

Atmospheric
Measurement
Techniques
Discussions

Open Access
EGU

440   (Fig. S2) revealing persistent dust layers associated with volume linear depolarization ratio (VLDR)

441   values of 5-10% at 355 nm, stretched from altitudes close to the ground and up to almost 6 km.

442   This case is ideal for evaluating L2A backscatter retrievals since non-spherical mineral

443   particles are probed by ALADIN, which does not detect the cross-polar component of the

444   backscattered lidar signal. Therefore, a degradation of ALADIN's performance is expected (i.e.,

445   underestimation of the backscatter coefficient and overestimation of the lidar ratio) when aspherical

446   particles (e.g., dust, volcanic ash, cirrus ice crystals) are probed. In Figure 3, the backscatter

447   coefficient step-like vertical profiles from Aeolus at the regular (brown) and mid-bin (black) vertical

448   scales are compared against those acquired by the Polly^{XT} (pink) at 355 nm. The colored dashed lines

449   (Aeolus) and the pink shaded area (Polly^{XT}) correspond to the statistical uncertainty margins of the

450   spaceborne and the ground-based (D'Amico et al., 2016) retrievals, respectively. At a first glance, it

451   is revealed that the geometrical structure of the dust layer, extending from 1 to 6 km, is generally well

452   captured by ALADIN (except at altitude ranges from 1 to 2.5 km), but the backscatter magnitude is

453   constantly underestimated. A fairer comparison, considering that depolarizing particles are recorded,

454   requires the conversion of the backscatter retrievals assuming that Polly^{XT} emits circularly polarized

455   radiation (instead of linearly polarized) and thus resembling ALADIN. Under the assumption of

456   randomly oriented particles and negligible multiple scattering effects, this transformation is made

457   based on theoretical formulas (Mishchenko and Hovenier, 1995; Roy and Roy, 2008), as it has been

458   shown in Paschou et al. (2021). Following this approach, the Aeolus-like backscatter (i.e., circular

459   co-polar component; blue curve in Fig. 3) is reproduced for the ground-based profiles at altitudes

460   where UV depolarization measurements are available. Thanks to this conversion, the Aeolus-Polly^{XT}

461   negative biases diminish and the Aeolus-like curve resides closer to those of SCA (brown) and SCA

462   mid-bin (black) backscatter levels. The difference between pink and blue backscatter profiles, ranging

463   from 13 to 33% in this specific case, reflects the underdetermination of the particle backscatter

464   coefficient in case of depolarizing aerosols being probed, due to the missing cross-polar backscatter

465   component.

466

467   *6.1.2 Long-range transport of anthropogenic aerosols on 3rd July 2019*

468   Under the prevalence of the Etesian winds (Tyrlis and Lelieveld, 2013), a typical pattern

469   dominating over the broader Greek area during summer months, when winds blow mainly from N-

470   NE directions, anthropogenic aerosols from megacities (Kanakidou et al., 2011) and particles

471   originating from biomass burning in the eastern Europe and in the surrounding area of the Black Sea

472   (van der Werf et al., 2017) are transported southwards. Based on the FLEXPART simulations (Fig.

473   S8), the air masses carrying fine particles, gradually descend till their arrival over Antikythera from

474　north-northeastern directions. During early morning hours, when ALADIN probes the atmosphere at

475　a distance of ~90 km westwards of the ground station (dawn orbit; descending), moderate AODs (up

476　to 0.15 at 340 nm) and very high Ångström exponent values (>1.2) are measured with the Cimel

477　sunphotometer (Fig. S5). The aerosol load is confined below 2.5 km consisting of spherical particles

478　as it is revealed from the Polly^{XT} volume linear depolarization ratio (VLDR) values, which do not

479　exceed 5% at 355 nm (Fig. S6). In the vicinity of the PANGEA observatory, MERRA-2 (Fig. S7-i)

480　and CAMS (Fig. S7-ii) AODs, mainly attributed to organic carbon, sulphate and sea-salt aerosols, do

481　not exceed 0.2 and they are coherent in spatial terms (i.e., horizontal homogeneity). In this case,

482　Polly^{XT} particle backscatter coefficient profiles coincide with the corresponding Aeolus-like profiles

483　(blue and pink curves are almost overlaid in Fig. 3-ii) since depolarization values are negligible.

484　Under these conditions, ALADIN is capable of reproducing satisfactorily the layer's structure (SCA

485　retrievals - brown curve) whereas slightly overestimates its intensity (SCA mid-bin retrievals - black

486　curve) with respect to the ground-truth retrievals.

487

488　*6.1.3 Long range transport of fine aerosols on 8th July 2020*

489　　　　On 8th July 2020, the broader area of the Antikythera island was under the impact of moderate-

490　to-high aerosol loads, mainly consisting of organic and sulphate particles based on CAMS simulated

491　AODs (up to 0.5) in the western and southern sector of the station (Fig. S11-ii). The prevalence of

492　fine aerosols is confirmed by the AERONET measurements, yielding UV AODs up to 0.5 and

493　Ångström exponent higher than 1.5 during early afternoon (Fig. S9). MERRA-2 AOD patterns (Fig.

494　S11-i) and speciation (strong contribution from marine and sulphate aerosols to the total aerosol load)

495　are different from those of CAMS, indicating a moderate performance with respect to the ground-

496　based sunphotometer observations (Fig. S9). Air masses originating in northern Balkans and the

497　Black Sea, after crossing metropolitan areas (i.e., Istanbul, Athens), are advected over ANT at

498　altitudes up to 4 km above surface, whereas a second cluster aloft (>5 km) indicates the convergence

499　of air masses from northwest (Fig. S12). In vertical terms, aerosol layers with local backscatter

500　maxima gradually reducing from 3.5 to 1.5 Mm^{-1} sr^{-1} are observed up to 4 km based on Polly^{XT}

501　backscatter coefficient profiles (pink curve, Fig. 3-iii) whereas almost identical values are recorded

502　for the Aeolus-like retrievals (blue curve, Fig. 3-iii). Aeolus performance reveals an altitude

503　dependency according to the comparison versus Polly^{XT} vertically resolved retrievals. From top to

504　bottom, the weak layer, extending from 6 to 8 km, observed in the ground-based lidar profiles is

505　partially evident in the Aeolus retrievals. At height ranges (< 4 km) where the main portion of the

506　aerosol burden resides, there is a contradiction of ALADIN's performance clearly seen beneath and

507　above ~2 km. In the free troposphere, the retrieved backscatter by ALADIN is underestimated with

508   respect to Polly^{XT} retrievals whereas the position of the Aeolus local maximum backscatter (~1 Mm$^-$

509   ^{1} sr^{-1}) is recorded exactly above the top of the aerosol layer observed from the ground. On the contrary,

510   below 2 km, the agreement between ALADIN and Polly^{XT} becomes better, particularly for SCA mid-

511   bin, even though the narrow peak recorded at ~1.2 km by Polly^{XT} cannot be reproduced by ALADIN.

512   This might be attributed either to the adjusted RBS at the lowermost bin (1 km thickness) or to the

513   lower accuracy of Aeolus retrievals near the ground due to the attenuation from the overlying layers

514   (Flament et al., 2021).

515

516   *6.1.4 Stratification of spherical and non-spherical particles on 5th August 2020*

517   In the last case, that took place on 5th August 2020, we are investigating the ability of Aeolus

518   to reproduce adequately the vertical structure of an aerosol layer detected up to 4 km based on Polly^{XT}

519   (Fig. 3-iv; pink curve). The "peculiarity" of this study case, as it is revealed by the Polly^{XT} time-

520   height plots of VLDR (Fig. S14), is that spherical fine particles dominate below 2.5 km whereas the

521   presence of non-spherical coarse aerosols above this layer is evident. This stratification results from

522   the convergence of air masses either originating in central Europe or suspending most of their travel

523   above northwest Africa (Fig. S12). According to MERRA-2 (Fig. S11-i) and CAMS (Fig. S11-ii)

524   reanalysis datasets, AODs fade from west to east while both numerical products indicate the

525   coexistence of carbonaceous, sulphate and mineral particles over the area where ALADIN samples

526   the atmosphere (~100 km westwards of Antikythera). During the Aeolus overpass (~04:40 UTC),

527   sunphotometer columnar observations are not available (Fig. S13). However, one hour later, UV

528   AODs up to 0.4 are recorded and remain relatively constant during sunlight hours. At the same time,

529   intermediate Ångström values (0.7 – 1), exhibiting weak temporal variation, indicate a mixing state

530   of fine and coarse aerosols. In the lowest troposphere (< 2km), Aeolus overestimates significantly the

531   backscatter coefficient but reproduces satisfactorily the aerosol layer structure at the mid-bin vertical

532   scale (i.e., SCA mid-bin; black curve; Fig. 3-iv), in contrast to the regular scale (i.e., SCA; brown

533   curve; Fig. 3-iv). It is reminded that SCA backscatter is actually retrieved whereas the SCA mid-bin

534   results by averaging two consecutive bins following the procedure applied on the extinction for

535   mitigating the downwards error propagation in the retrieval algorithm solution (Flament et al., 2021).

536   At higher altitudes (2.5 – 4 km), due to the suspension of depolarizing mineral particles, a declination

537   is marked between the pink (linear-derived) and blue (Aeolus-like) Polly^{XT} profiles. Again, the SCA

538   mid-bin backscatter performs better than those of SCA reproducing more realistically the shape and

539   the magnitude of the Polly^{XT} Aeolus-like profile. Finally, ALADIN detects aerosol layers between

540   5.5 and 8 km, assuming that clear-sky conditions are appropriately represented in the MSG-SEVIRI

Atmospheric
Measurement
Techniques
Discussions

Open Access

EGU

541 imagery and remain constant within the time interval (~6 minutes) of MSG and Aeolus observations,

542 and the SCA mid-bin backscatter resides closer to the Polly^{XT} levels, which, however, are noisy.

543   A general remark that should be made, is that for the cases analyzed, between the ground-

544 based and spaceborne profiles there is an inconsistency in the vertical representativeness within the

545 lowermost Aeolus bin. Under the absence of the near-field receivers (not considered in our study)

546 Polly^{XT} profiles are reported above ~800 m where the overlap between the laser beam and the receiver

547 telescope field of view is expected to be full. However, the base altitude of the near-surface Aeolus

548 bin is at ~200 m. This can interpret, at some degree, the large positive ALADIN-Polly^{XT} departures

549 at altitudes below 1 km, which are possibly further strengthened by an inappropriate RBS (i.e., low

550 SNR) in the Aeolus retrievals.

551

552 *6.2 Overall assessment and dependencies*

553   In the second part of the analysis, an overall assessment of the Aeolus L2A retrievals is

554 performed. Due to the very limited availability of ground-based extinction profiles, only the Aeolus

555 L2A backscatter observations are evaluated. It must be clarified that the evaluation of the Aeolus

556 satellite (SAT) backscatter coefficient is conducted without any conversion (i.e., from total linear to

557 circular co-polar) of the ground-based lidar (GRD) profiles. This has been decided since many of the

558 SAT-GRD collocated samples are derived from the Thessaloniki station. Due to technical issues

559 (related to the polarization purity of the emitted laser beam and the performance of the telescope

560 lenses) no calibrated depolarizing measurements, necessary to derive the Aeolus-like products

561 (Paschou et al., 2021), are available for the study period. Nevertheless, we are not expecting that this

562 consideration, acknowledging that it is imperfect, will affect substantially the robustness of our

563 findings since in most of the study cases the contribution of depolarizing particles is quite low based

564 on the ancillary datasets/products. The discussion in the current section is divided in two parts. First,

565 the vertically resolved evaluation metrics are presented separately for the two Aeolus vertical scales,

566 both for the unfiltered and the filtered (cloud-free) profiles (Section 6.2.1). The same analysis format

567 (i.e., SCA vs SCA mid-bin, unfiltered vs filtered) is kept in the second sub-section (Section 6.2.2)

568 where the evaluation results are presented as a function of various dependencies.

569

570 *6.2.1 Vertically resolved evaluation metrics*

571   In Figure 4, the vertically resolved bias (SAT-GRD; upper panel) and root mean square error

572 (RMSE; bottom panel) metrics are depicted for the unfiltered (cloud and aerosol backscatter) Aeolus

573 L2A backscatter retrievals, reported at the regular (left column) and the mid-bin (right column)

574 vertical scales. Bias and RMSE metrics are used in a complementary way in order to avoid any

575   misleading interpretation of the former score attributed to counterbalancing negative and positive

576   SAT-GRD deviations. For the calculation of the evaluation scores, the GRD profiles have been

577   rescaled to match Aeolus vertical product resolution. Note that in the SAT-GRD pairs, all BRCs from

578   all cases are included (right y-axis in Figure 4), satisfying the defined collocation criteria (see Section

579   5), and they are treated individually. Aeolus L2A data are provided vertically at a constant number of

580   range bins (i.e., 24 for SCA and 23 for SCA mid-bin) but their base altitude and their range vary along

581   the orbit and from orbit-to-orbit and they are defined dynamically (depending on the optimum SNR).

582   Therefore, since the GRD and SAT profiles are not interpolated in a common predefined grid, we are

583   using as reference the reverse index (with respect to those considered in the SCA retrieval algorithm

584   in which 1 corresponds to the top-most bin) of Aeolus SCA (from 1 to 24; left y-axis in Figs 4 i-a and

585   ii-a) and SCA mid-bin (from 1 to 23; left y-axis in Figs 4 i-b and ii-b) vertical scales.

586   According to our results for the unfiltered Aeolus backscatter profiles (Fig. 5), positive biases

587   (up to 3.5 Mm^{-1} sr^{-1}; red bars) are evident, at both vertical scales, at the first three bins (below 2 km).

588   For altitude ranges spanning from 2 to 8 km (bins 4 – 12), mainly positive SAT-GRD biases (up to

589   ~1.5 Mm^{-1} sr^{-1}) are recorded for SCA mid-bin whereas for SCA reach up to ~1 Mm^{-1} sr^{-1} in absolute

590   terms. Similar tendencies are evident at the highest altitudes (> 8 km) but the magnitude of the SAT-

591   GRD offsets becomes lower (< 0.5 Mm^{-1} sr^{-1}). Between the two Aeolus vertical scales, SCA mid-bin

592   performs better than SCA up to ~8 km (bin 12) and similar aloft, as it is shown by the RMSE profiles

593   (bottom panel in Fig. 4). Nevertheless, the most important finding is that Aeolus is not capable to

594   reproduce satisfactorily the backscatter profiles as it is revealed by the RMSE levels, which are

595   maximized near the ground (~ 8 Mm^{-1} sr^{-1}), are considerably high (up to 6 Mm^{-1} sr^{-1}) in the free

596   troposphere and are minimized (< 1 Mm^{-1} sr^{-1}) at the uppermost bins. Our findings are highly

597   consistent with those presented in Abril-Gago et al. (2022), who performed a validation of Aeolus

598   L2A particle backscatter coefficient against reference measurements obtained at three

599   ACTRIS/EARLINET sites in the Iberian Peninsula. Several factors contribute to the obtained height-

600   dependen SAT-GRD discrepancies. Near the ground, the observed maximum overestimations are

601   mainly attributed to the: (i) contamination of the ALADIN lidar signal by surface reflectance, (ii)

602   increased noise in the lowermost bins and (iii) limited vertical representativeness of the GRD profiles

603   below 1 km. On the contrary, in the free troposphere, the cloud contamination on spaceborne

604   retrievals plays a dominant role on the occurrence of ALADIN backscatter overestimations with

605   respect to the cloud-free ground-based retrievals. From a statistical point of view, it must also be

606   mentioned that the robustness of the bias and RMSE metrics decreases for the increasing altitudes

607   due to the reduction of the number of the SAT-GRD matchups (right y-axis in Fig. 4) participating in

608   the calculations.

609   The assessment analysis has been repeated after removing Aeolus profiles when clouds are

610   detected by MSG-SEVIRI (grey shaded areas in Fig. 1) within a BRC (colored rectangles in Fig. 1).

611   By contrasting Figures 4 and 5 (evaluation metrics for the filtered profiles), an expected improvement

612   of the level of agreement between SAT and GRD is visible. This translates into a drastic reduction of

613   bias and RMSE values at altitude ranges up to 5-6 km (~bin 12). Between bins 2 and 5 slight

614   underestimations (blue bars) and overestimations (red bars) are found for SCA (Fig. 5 i-a) whereas

615   low positive SAT-GRD offsets are recorded for SCA mid-bin (Fig. 5 i-b). Above bin 5, SAT-GRD

616   deviations are low in absolute terms, oscillating around zero, for SCA, whereas only positive SAT-

617   GRD biases are recorded for SCA mid-bin, which are maximized (~ 0.7 Mm^{-1} sr^{-1}) at the highest bins

618   and are associated with limited SAT-GRD matchups (right x-axis in Fig. 5 i-b). The obtained

619   improvements on bias scores become more confident since they are associated with similar strong

620   reductive tendencies on RMSE levels. More specifically, the RMSE spikes of extremely high values

621   recorded in the unfiltered profiles either disappear or weaken in the case of the Aeolus filtered SCA

622   (Fig. 5 ii-a) and SCA mid-bin (Fig. 5 ii-b) backscatter profiles. However, even though the RMSE

623   values at the lowermost bins are decreased when cloud contaminated Aeolus profiles are eliminated,

624   still the corresponding levels for the filtered profiles are considerably high attributed to the higher

625   SNR and the possible impact of surface returns.

626

6.2.2 Scatterplots

628

629   An alternative approach to assess the performance of Aeolus L2A backscatter is attempted

630   here by reproducing two dimensional histograms for the entire SAT-GRD collocated sample as well

631   as scatterplots resolved based on various dependencies, aiming to investigate the factors determining

632   the level of agreement between spaceborne and ground-based retrievals. More specifically, the

633   dependencies under investigation are those of the: (i) station locations, (ii) BRCs and (iii) orbits (dawn

634   vs dusk). The evaluation metrics have been calculated for all possible combinations of vertical scales

635   (SCA vs SCA mid-bin) and Aeolus profiles (unfiltered vs filtered).

636   Figure 6 depicts the two-dimensional histograms between GRD (x-axis) and SAT (y-axis)

637   backscatter coefficient for the raw (upper panel) and filtered (bottom panel) Aeolus profiles reported

638   at the SCA (left column) and SCA mid-bin (right column) vertical scales. Note that we have removed

639   SAT-GRD pairs in which Aeolus backscatter exceeds 20 Mm^{-1} sr^{-1} in order to avoid the

640   "contamination" of extreme outliers in the calculated metrics, possibly attributed to the presence of

641   clouds (Proestakis et al., 2019). It is also clarified that the Aeolus QA flags are not taken into account

642   in the current study, since their validity is not yet reliable (Reitebuch et al., 2020) as it has been

643   demonstrated in Abril-Gago et al. (2022).

644   Between SCA and SCA mid-bin unfiltered retrievals there is a contradiction of which
645 performs better relying on the correlation coefficient (0.36 and 0.39, respectively), bias (0.45 and
646 0.69, respectively) and RMSE (2.00 and 1.88, respectively) metrics. After removing cloud-
647 contaminated Aeolus profiles, the amount of the SAT-GRD matchups is reduced by about 55% and
648 59% for SCA (from 537 to 239) and SCA mid-bin (from 356 to 147), respectively. Nevertheless,
649 thanks to this filtering procedure, the initially observed overestimations for SCA and SCA mid-bin
650 are reduced by ~25% and ~43%, respectively, whereas the RMSE values drop down to 1.65 (SCA)
651 and 1.00 (SCA mid-bin). The better agreement between SAT and GRD, for the filtered Aeolus
652 profiles, is further justified by the increase of the R values (from 0.39 to 0.48) for the SCA mid-bin
653 whereas for SCA there is not any positive or negative tendency (R=0.36). The spread of the points in
654 the two dimensional space reveals many similarities with the corresponding scatterplots presented in
655 Abril-Gago et al. (2022) for the Iberian ACTRIS/EARLINET stations.

656   A common feature in all scatterplots, shown in Figure 6, is that most of the positive outliers
657 are found at the lowermost bins (see Figs. 4 and 5). SAT beta can reach up to 20 Mm^{-1} sr^{-1} in contrast
658 to the corresponding GRD levels, which are mainly lower than 2 Mm^{-1} sr^{-1}. For SCA (Figs. 6 i-a, 6
659 ii-a), the majority of the negative SAT-GRD pairs are recorded at the highest bins in which, however,
660 both spaceborne and ground-based backscatter coefficients are noisy. Another cluster of SAT-GRD
661 pairs is those where slight negative Aeolus backscatter values are grouped together with low positive
662 backscatter values retrieved from ground. At the mid-bin vertical scale, for the unfiltered Aeolus
663 profiles (Fig. 6 i-b), the negative SAT backscatter values are masked out resulting in better evaluation
664 metrics (except the increase of bias due to the removal of the negative Aeolus backscatter) with
665 respect to the regular vertical scale. Among the four scatterplots, the best agreement between Aeolus
666 and ground-based retrievals is revealed for the SCA mid-bin filtered profiles (Fig. 6 ii-b) attributed
667 to the coincident elimination of the negative and the extreme positive Aeolus backscatter coefficient.

668   Figure 7 depicts the overall scatterplot between ground-based and spaceborne retrievals as a
669 function of the three PANACEA sites (colored categories). The associated evaluation scores are
670 summarized in Table 1 and 2 for the unfiltered and filtered Aeolus profiles, respectively. The majority
671 of the extreme positive outliers of unfiltered SCA retrievals (Fig. 7 i-a) are recorded in Thessaloniki
672 and Athens. According to our results, significant overestimations (0.73 for ATH and 0.83 for THE)
673 and high RMSE values (2.26 for ATH and 2.60 for THE) are found. At Antikythera island (ANT),
674 the biases are quite low and equal to 0.06 and 13.6% in absolute and relative terms, respectively
675 (Table 1). In all stations, for the unfiltered SCA mid-bin retrievals, the absolute SAT-GRD departures
676 become larger whereas the RMSE decreases in ANT/THE and increases in ATH. Regarding the
677 temporal covariation between SAT and GRD retrievals, a noticeable improvement is evident in ANT

678   (i.e., R increases from 0.49 to 0.57). For the quality-assured Aeolus profiles (Table 2), all evaluation

679   metrics converge towards the ideal scores for SCA mid-bin whereas mainly positive tendencies (i.e.,

680   better agreement) are evident for SCA. Overall, among the three stations the best performance of

681   Aeolus is recorded at Antikythera island.

682   Between dawn (descending) and dusk (ascending) orbits, better bias and RMSE scores are

683   computed when Aeolus is flying during early morning hours while better R values are found during

684   early afternoon satellite overpasses. However, our orbit-based results are not robust since the number

685   of Aeolus overpasses is not evenly distributed (about 85% of the SAT-GRD matchups are acquired

686   during dawn orbits). Among the three BRCs (red, blue or magenta), which can satisfy the defined

687   SAT-GRD spatial criterion (see Section 5) the best metrics are found for the red BRC residing closer

688   to the station site.

689

690   **7. Discussion on Cal/Val aspects and recommendations**

691

692   Throughout this assessment analysis, several critical points have been identified and

693   highlighted that should be addressed adequately towards a comprehensive Cal/Val study of the

694   Aeolus L2A aerosol products. These aspects, summarized in the current section, can: (i) serve as

695   guidelines for future relevant studies, (ii) improve our understanding about the advantages/limitations

696   of Aeolus data in terms of their usefulness and applicability in aerosol-related studies and (iii) suggest

697   possible upgrades regarding ALADIN's observational capabilities, the considerations of the applied

698   retrieval algorithms and the content of information in Aeolus L2A data.

699   A fair comparison of Aeolus L2A backscatter versus linear-derived retrievals acquired from

700   ground-based lidars, when depolarizing particles are recorded, requires the conversion of the latter

701   ones to circular co-polar (Aeolus-like) following Paschou et al. (2021). Nevertheless, it should be

702   acknowledged that the theoretical assumptions can be invalid either due to the orientation of the

703   suspended particles (e.g., mineral dust; Ulanowski et al., 2007; Daskalopoulou et al., 2021; Mallios

704   et al., 2021) or due to multiple scattering effects within optically thick aerosol layers (Wandinger et

705   al., 2010). The lack of discrimination between aerosols and clouds in Aeolus L2A data forces the

706   synergistic implementation of ancillary data in order to remove cloud contaminated Aeolus profiles

707   from the collocated sample with the cloud-free ground-based profiles. Nevertheless, it should be

708   noted that the cloud removal itself is not perfect. In our case, we are relying on MSG-SEVIRI cloud

709   observations, which are available at high temporal frequency (every 15 min) thus allowing a very

710   good temporal collocation with Aeolus. The indirect cloud-mask filtering applied to our analysis,

711   leads to a substantial improvement of the level of agreement between spaceborne and ground-based

Atmospheric
Measurement
Techniques
Discussions

EGU
Open Access

712 retrievals. Despite its success, our proposed approach provides a sufficient and acceptable solution,
713 but undoubtedly cannot be superior to the utility of a descriptive classification scheme on Aeolus
714 retrieval algorithms similarly done in CALIOP-CALIPSO (Liu et al., 2019; Zeng et al., 2019).

715 Aeolus retrievals are available at coarse along-track resolution (~90 km). This imposes
716 limitations on their evaluation against point measurements, which are further exacerbated at sites
717 where the heterogeneity of aerosol loads in the surrounding area of the station is pronounced, taking
718 into account that the spatial collocation between spaceborne and ground-based retrievals is not exact.
719 Numerical outputs from reanalysis datasets (e.g., MERRA-2, CAMS) can be utilized as an indicator
720 of aerosols' burden horizontal variation, taking advantage of their complete spatial coverage, their
721 availability at high temporal frequency and their reliability (Innes et al., 2019; Gueymard and Yang,
722 2020). Over areas with a complex terrain, due to the coarse BRC horizontal resolution, they can be
723 recorded vertical inconsistencies between ground-based and satellite profiles (reported above ground
724 where its height is defined with respect to the WGS 84 ellipsoid), not physically explained. For the
725 derivation of the evaluation scores, it is required a rescaling of the ground-based profiles, acquired at
726 finer vertical resolution, in order to match the dynamically defined Aeolus' range bin settings.
727 Nevertheless, due to this transformation, the shape of the raw ground-based profile can be distorted
728 and the magnitude of the retrieved optical properties can be modified substantially thus affecting the
729 evaluation metrics. This artifact is evident in cases where the vertical structure of the aerosol layers
730 is highly variable thus hindering Aeolus capability to reproduce accurately their geometrical features
731 due to the coarse vertical resolution in which optical products are derived. Finally, the consideration
732 of backward trajectories can assist the characterization of the probed atmospheric scene by Aeolus.
733 Potentially, they can be also used as an additional criterion for the optimum selection of Aeolus BRC
734 for the collocation with the ground-based measurements. However, possible limitations may arise due
735 to temporal deviations among FLEXPART run, the Aeolus overpass and ground-based retrievals,
736 which might be critical taking into account the strong spatiotemporal variability of aerosol loads
737 across various scales.

738

8. Conclusions

740 The limited availability of vertically resolved aerosol products from space constitutes a major
741 deficiency of the Global Observing System (GOS). The launch of the Aeolus ESA satellite was a
742 major step towards this direction whereas the forthcoming EarthCARE satellite mission (Illingworth
743 et al., 2015) will accelerate further these efforts. ALADIN, the single payload of the Aeolus satellite,
744 constitutes the first UV HSRL Doppler lidar ever placed in space and it is optimized to acquire HLOS
745 wind profiles towards advancing numerical weather prediction (Rennie et al., 2021). ALADIN also

Atmospheric
Measurement
Techniques
Discussions

Open Access

EGU

746   retrieves independently the extinction and backscatter coefficients of aerosols and clouds (grouped as

747   particulates according to Aeolus' nomenclature) via the implementation of the SCA algorithm.

748   The current work focuses on the assessment analysis of L2A particle backscatter coefficients

749   versus ground-based retrievals acquired routinely by lidar systems operating in Athens, Thessaloniki,

750   and Antikythera. The aforementioned stations contribute to the PANACEA Greek National Research

751   Infrastructure (Greek ACTRIS component) and to the European Aerosol Research Lidar Network

752   (EARLINET; Pappalardo et al., 2014). Overall, 46 cases are analyzed out of which 12 have been

753   identified in the urban site of Athens, 16 in Thessaloniki and 15 in the remote site of the Antikythera

754   island.

755   In the first part of the analysis, focus was given on the assessment of Aeolus L2A particle

756   backscatter coefficient, under specific aerosol scenarios, versus the corresponding measurements

757   obtained at the Antikythera island (southwest Greece). As expected, the misdetection of the cross

758   polarized lidar return signals, induces an underestimation of Aeolus L2A backscatter when

759   depolarizing mineral particles are probed. By converting the ground-based linear-derived total

760   backscatter to circular co-polar (i.e., Aeolus-like) it is computed that these underestimations range

761   from 13% to 33% (case of 10th July 2019). For the case of 3rd July 2019, when aerosol loads of

762   moderate intensity, consisting mainly of spherical particles, are confined below 4 km and they are

763   homogeneous in the surrounding area of the station, Aeolus is capable in reproducing quite well the

764   ground-based profile in terms of shape and magnitude. On the contrary, in the case of 8th July 2020,

765   when the stratification of aerosol layers, detected up to 4 km by Polly^{XT}, becomes complex, Aeolus'

766   performance reveals an altitude dependency, probably attributed to the coarse vertical sampling of

767   the atmosphere. Finally, the agreement between Aeolus and Polly^{XT} backscatter retrievals varies with

768   height on 5th August 2020 when non-spherical particles (2-4 km) reside on top of a layer consisting

769   of spherical aerosols.

770   From our statistical assessment analysis, it has been revealed that the removal of cloud

771   contaminated spaceborne profiles, achieved via the synergy with MSG-SEVIRI cloud observations,

772   results in a significant improvement of the product performance. Unfortunately, the poor evaluation

773   metrics at the lowermost bins (attributed to either the surface reflectance or the increased noise levels

774   for the Aeolus retrievals and to the overlap issues for the ground-based profiles) are still evident after

775   the cloud filtering procedure. Between the two Aeolus vertical scales, the computed evaluation

776   metrics do not provide strong evidence of which of them performs better. Among the three stations

777   (ATH, ANT, THE) considered here, the best agreement was found in the remote site of Antikythera

778   island (spatially homogeneous AODs) in contrast to the urban sites of Athens and Thessaloniki. All

779 key cal/val aspects have been discussed thoroughly serving as guidelines and potential
780 recommendations for future studies.

781   The lack of the cross-polar channel downgrades ALADIN's performance under depolarizing
782 atmospheric scenes (e.g., dust, cirrus crystals, volcanic ash) hampering an effective aerosols/clouds
783 discrimination (Flamant et al., 2021). According to preliminary CAMS assimilation experiments
784 (A3S), relying on Aeolus L2A backscatter, it has been demonstrated to have a beneficial impact on
785 short-term forecasts. However, it is under investigation if the inclusion of the cross-polar channel will
786 expand these positive feedbacks on NWP (main scientific goal of the Aeolus satellite mission), taking
787 into account that aerosol-radiation interactions affect atmospheric dynamics and vice-versa. Another
788 important aspect is the coarse resolution of Aeolus L2A retrievals, both in horizontal and vertical,
789 imposing several limitations in an appropriate assessment analysis whereas it can be critical in their
790 implementation on other applications (e.g. data assimilation).

791   In the current study, we emphasized only on the particle backscatter coefficient due to the
792 limited number of ground-based extinction profiles. A wider assessment analysis is ongoing in the
793 framework of the Aeolus L2A Cal/Val study performed within EARLINET. Taking into account the
794 challenges that the SCA algorithm faces in retrieving the extinction coefficient reliably (Flament et
795 al., 2021), new retrievals will become available in the Aeolus L2A product. These include the
796 Maximum Likelihood Estimate (MLE) (Ehlers et al., 2021) and the EarthCARE derived AEOL-FF
797 and AEL-PRO products (refer to the latest L2A product release documentation). Finally, the best
798 assessment of Aeolus L2A products is expected versus the purpose-built eVe lidar (Paschou et al.,
799 2021) implemented in a dual-laser/dual-telescope configuration enabling the simultaneous emission
800 of linearly and circularly polarized radiation at 355 nm and the detection of the elastically
801 backscattered radiation with polarization sensitive channels as well as the inelastic (Raman)
802 backscattered radiation at 387 nm. As such, eVe can mimic Aeolus' observational geometry and test
803 the validity of the theoretical formulas applied for the derivation of the Aeolus-like backscatter from
804 the linearly polarized emission ground-based systems. The first correlative Aeolus-eVe
805 measurements have been performed in the framework of the Joint Aeolus Tropical Atlantic Campaign
806 (JATAC), that took place in Cape Verde in September 2021. Correlative measurements are also
807 planned in June 2022 at the same place during the ESA-ASKOS experimental campaign. The
808 geographical location of Cape Verde, situated on the "corridor" of the Saharan transatlantic transport
809 (Gkikas et al., 2022), is ideal for assessing Aeolus performance when non-spherical mineral particles
810 from the nearby deserts are advected westwards.

811

812

Atmospheric
Measurement
Techniques

Discussions

830

831 **Data availability**

832 Aeolus Baseline 10 and 11 L2A data were obtained from the ESA Aeolus Online Dissemination

833 System available at https://aeolus-ds.eo.esa.int/oads/access/.

834

835 **References**

836 Abril-Gago, J., Guerrero-Rascado, J. L., Costa, M. J., Bravo-Aranda, J. A., Sicard, M., Bermejo-

837 Pantaleón, D., Bortoli, D., Granados-Muñoz, M. J., Rodríguez-Gómez, A., Muñoz-Porcar, C.,

838 Comerón, A., Ortiz-Amezcua, P., Salgueiro, V., Jiménez-Martín, M. M., and Alados-Arboledas, L.:

839 Statistical validation of Aeolus L2A particle backscatter coefficient retrievals over

840 ACTRIS/EARLINET stations on the Iberian Peninsula, Atmos. Chem. Phys., 22, 1425–1451,

841 https://doi.org/10.5194/acp-22-1425-2022, 2022.

842

843 Amiridis, V., Balis, D. S., Giannakaki, E., Stohl, A., Kazadzis, S., Koukouli, M. E., and Zanis, P.:

844 Optical characteristics of biomass burning aerosols over Southeastern Europe determined from UV-

845 Raman lidar measurements, Atmos. Chem. Phys., 9, 2431–2440, https://doi.org/10.5194/acp-9-2431-
846 2009, 2009.

847

848 Amiridis, V., Giannakaki, E., Balis, D. S., Gerasopoulos, E., Pytharoulis, I., Zanis, P., Kazadzis, S.,
849 Melas, D., and Zerefos, C.: Smoke injection heights from agricultural burning in Eastern Europe as
850 seen by CALIPSO, Atmos. Chem. Phys., 10, 11567–11576, https://doi.org/10.5194/acp-10-11567-
851 2010, 2010.

852

853 Amiridis, V., Zerefos, C., Kazadzis, S., Gerasopoulos, E., Eleftheratos, K., Vrekoussis, M., Stohl, A.,
854 Mamouri, R.E., Kokkalis, P., Papayannis, A., et al.: Impact of the 2009 Attica wildfires on the air
855 quality in urban Athens, Atmos. Environ., 46, 536–544,
856 https://doi.org/10.1016/j.atmosenv.2011.07.056, 2012.

857

858 Amodeo, Aldo, D'Amico, Giuseppe, Giunta, Aldo, Papagiannopoulos, Nikolaos, Papayannis, Alex,
859 Argyrouli, Athina, Mylonaki, Maria, Tsaknakis, Georgios, Kokkalis, Panos, Soupiona, Ourania,
860 Tzanis, Chris. (2018). ATHLI16: the ATHens Lidar Intercomparison campaign. EPJ Web of
861 Conferences. 176. 09008. 10.1051/epjconf/201817609008.

862

863 Ansmann, A., Petzold, A., Kandler, K., Tegen, I., Wendisch, M., Müller, D., Weinzierl, B., Müller,
864 T. and Heintzenberg, J.: Saharan Mineral Dust Experiments SAMUM–1 and SAMUM–2: what have
865 we learned?, Tellus B: Chemical and Physical Meteorology, 63(4), 403–429, doi:10.1111/j.1600-
866 0889.2011.00555.x, 2011.

867

868 Ansmann, A., Wandinger, U., Riebesell, M., Weitkamp, C., Michaelis, W.: Independent measurement
869 of extinction and backscatter profiles in cirrus clouds by using a combined raman elastic-backscatter
870 lidar, Applied Optics, 31, 7113-7131, doi: 10.1364/AO.31.007113, 1992.

871

872 Baars, H., et al. : An overview of the first decade of PollyNET: an emerging network of automated
873 Raman-polarization lidars for continuous aerosol profiling, Atmos. Chem. Phys., 16, 5111–5137,
874 https://doi.org/10.5194/acp-16-5111-2016, 2016.

875

876 Baars, H., Ansmann, A., Ohneiser, K., Haarig, M., Engelmann, R., Althausen, D., Hanssen, I., Gausa,
877 M., Pietruczuk, A., Szkop, A., Stachlewska, I. S., Wang, D., Reichardt, J., Skupin, A., Mattis, I.,
878 Trickl, T., Vogelmann, H., Navas-Guzmán, F., Haefele, A., Acheson, K., Ruth, A. A., Tatarov, B.,

879   Müller, D., Hu, Q., Podvin, T., Goloub, P., Veselovskii, I., Pietras, C., Haeffelin, M., Fréville, P.,

880   Sicard, M., Comerón, A., Fernández García, A. J., Molero Menéndez, F., Córdoba-Jabonero, C.,

881   Guerrero-Rascado, J. L., Alados-Arboledas, L., Bortoli, D., Costa, M. J., Dionisi, D., Liberti, G. L.,

882   Wang, X., Sannino, A., Papagiannopoulos, N., Boselli, A., Mona, L., D'Amico, G., Romano, S.,

883   Perrone, M. R., Belegante, L., Nicolae, D., Grigorov, I., Gialitaki, A., Amiridis, V., Soupiona, O.,

884   Papayannis, A., Mamouri, R.-E., Nisantzi, A., Heese, B., Hofer, J., Schechner, Y. Y., Wandinger, U.,

885   and Pappalardo, G.: The unprecedented 2017–2018 stratospheric smoke event: decay phase and

886   aerosol properties observed with the EARLINET, Atmos. Chem. Phys., 19, 15183–15198,

887   https://doi.org/10.5194/acp-19-15183-2019, 2019.

888

889   Baars, H., Herzog, A., Heese, B., Ohneiser, K., Hanbuch, K., Hofer, J., Yin, Z., Engelmann, R., and

890   Wandinger, U.: Validation of Aeolus wind products above the Atlantic Ocean, Atmos. Meas. Tech.,

891   13, 6007–6024, https://doi.org/10.5194/amt-13-6007-2020, 2020.

892

893   Baars, H., Radenz, M., Floutsi, A. A., Engelmann, R., Althausen, D., Heese, B., Ansmann, A.,

894   Flament, T., Dabas, A., Trapon, D., Reitebuch, O., Bley, S., and Wandinger, U.: Californian wildfire

895   smoke over Europe: A first example of the aerosol observing capabilities of Aeolus compared to

896   ground-based   lidar,   Geophys.   Res.   Lett.,   48,   e2020GL092194,

897   https://doi.org/10.1029/2020GL092194, 2021.

898

899   Balis, D., Amiridis, V., Nickovic, S., Papayannis, A., and Zerefos, C.: Optical properties of Saharan

900   dust layers as detected by a Raman lidar at Thesaloniki, Greece, Geophys. Res. Lett., 31, L13104,

901   https://doi.org/10.1029/2004GL019881, 2004

902

903   Balis, D., Amiridis, V., Kazadzis, S., Papayannis, A., Tsaknakis, G., Tzortzakis, S., Kalivitis, N.,

904   Vrekoussis, M., Kanakidou, M., Mihalopoulos, N., Chourdakis, G., Nickovic, S., Pérez, C.,

905   Baldasano, J., and Drakakis, M.: Optical characteristics of desert dust over the East Mediterranean

906   during summer: a case study, Ann. Geophys., 24, 807–821, https://doi.org/10.5194/angeo-24-807-

907   2006, 2006.

908

909   Brioude, J., Arnold, D., Stohl, A., Cassiani, M., Morton, D., Seibert, P., Angevine, W., Evan, S.,

910   Dingwell, A., Fast, J.D., Easter, R.C., Pisso, I., Burkhart, J., Wotawa, G., 2013. The Lagrangian

911   particle dispersion model FLEXPART-WRF version 3.1. Geosci. Model. Dev. 6, 1889e1904.

912   http://dx.doi.org/10.5194/gmd-6-1889-2013.

913

914   Bohlmann, S., Baars, H., Radenz, M., Engelmann, R., and Macke, A.: Ship-borne aerosol profiling

915   with lidar over the Atlantic Ocean: from pure marine conditions to complex dust–smoke mixtures,

916   Atmos. Chem. Phys., 18, 9661–9679, https://doi.org/10.5194/acp-18-9661-2018, 2018.

917

918   Boucher, O., Randall, D., Artaxo, P., Bretherton, C., Feingold, G., Forster, P., Kerminen, V.-M.,

919   Kondo, Y., Liao, H., Lohmann, U., Rasch, P., Satheesh, S., Sherwood, S., Stevens, B., and Zhang,

920   X.: Clouds and Aerosols, in: Climate Change 2013: The Physical Science Basis. Contribution of

921   Working Group I to the Fifth Assessment Report of the Intergovernmental Panel on Climate Change,

922   edited by Stocker, T., Qin, D., Plattner, G.-K., Tignor, M., Allen, S., Boschung, J., Nauels, A., Xia,

923   Y., Bex, V., and Midgley, P., chap. 7, pp. 571–658, Cambridge University Press, Cambridge, United

924   Kingdom and New York, NY, USA, https://doi.org/10.1017/CBO9781107415324.016, 2013.

925

926   Buchard, V., Randles, C. A., da Silva, A. M., Darmenov, A., Colarco, P. R., Govindaraju, R., Ferrare,

927   R., Hair, J., Beyersdorf, A. J., Ziemba, L. D. and Yu, H.: The MERRA-2 aerosol reanalysis, 1980

928   onward.   Part   II: Evaluation   and   case   studies,   J.   Climate,   30,   6851–6872,

929   https://doi.org/10.1175/JCLI-D-16-0613.1, 2017.

930

931   Campbell, J. R., Hlavka, D. L., Welton, E. J., Flynn, C. J., Turner, D. D., Spinhirne, J. D., Scott, V.

932   S., and Hwang, I. H.: Full-time eye-safe cloud and aerosol lidar observation at Atmospheric Radiation

933   Measurement program sites: Instruments and data processing, J. Atmos. Oceanic Technol., 19, 431–

934   442, 2002.

935

936   Charlson, R. J., Schwartz, S. E., Hales, J. M., Cess, R. D., Coakley, J. A., Hansen, J. E., and Hofmann,

937   D.   J.:   Climate   Forcing   by   Anthropogenic   Aerosols,   Science,   255,   423–430,

938   https://doi.org/10.1126/science.255.5043.423, 1992.

939

940   Collis, R. and Russell, P.: Lidar measurement of particles and gases by elastic backscattering and

941   differential absorption, chap. Lidar measurement of particles and gases by elastic backscattering and

942   differential absorption, Springer, Berlin, Heidelberg, 71– 151, https://doi.org/10.1007/3-540-07743-

943   X_18, 1976.

944

Atmospheric
Measurement
Techniques
Discussions

Open Access

EGU

945   Dabas, A.: Generation of AUX_CAL: Detailed Processing Model and Input/Output Data Definition,

946   software, ESA, available at: https://earth.esa.int/eogateway/documents/20142/ 1564626/Aeolus-

947   Calibration-Processor-Documentation.zip (last access: 20 February 2022), 2017.

948

949   D'Amico, G., Amodeo, A., Mattis, I., Freudenthaler, V., and Pappalardo, G.: EARLINET Single

950   Calculus Chain – technical – Part 1: Pre-processing of raw lidar data, Atmos. Meas. Tech., 9, 491–

951   507, https://doi.org/10.5194/amt-9-491-2016, 2016.

952

953   Daskalopoulou, V., Raptis, I. P., Tsekeri, A., Amiridis, V., Kazadzis, S., Ulanowski, Z., Metallinos,

954   S., Tassis, K., and Martin, W.: Monitoring dust particle orientation with measurements of sunlight

955   dichroic extinction, 15th International Conference on Meteorology, Climatology and Atmospheric

956   Physics (COMECAP 2021), Ioannina, Greece, 26–29 September 2021, Zenodo [conference paper],

957   https://doi.org/10.5281/zenodo.5075998, 2021.

958

959   Derrien, M. and Le Gleau, H.: MSG/SEVIRI cloud mask and type from SAFNWC,   Int.   J.

960   Remote Sens., 26, 4707–4732, 2005.

961

962   ECMWF: ECMWF starts assimilating Aeolus wind data, https://www.ecmwf.int/en/about/media-

963   centre/news/2020/ecmwf-starts-assimilating-aeolus-wind-data, last access: 12 June 2020, 2020.

964

965   Engelmann, R., Kanitz, T., Baars, H., Heese, B., Althausen, D., Skupin, A., Wandinger, U.,

966   Komppula, M., Stachlewska, I. S., Amiridis, V., Marinou, E., Mattis, I., Linné, H., and Ansmann, A.:

967   The automated multiwavelength Raman polarization and water-vapor lidar Polly^{XT}: the neXT

968   generation, Atmos. Meas. Tech., 9, 1767–1784, https://doi.org/10.5194/amt-9-1767-2016, 2016.

969

970   Errera, Q., Y. Bennouna, M. Schulz, H.J. Eskes, S. Basart, A. Benedictow, A.-M. Blechschmidt, S.

971   Chabrillat, H. Clark, E. Cuevas, H. Flentje, K.M. Hansen, U. Im, J. Kapsomenakis, B. Langerock, K.

972   Petersen, A. Richter, N. Sudarchikova, V. Thouret, A. Wagner, Y. Wang, T. Warneke, C. Zerefos,

973   Validation report of the CAMS global Reanalysis of aerosols and reactive gases, years 2003-2020,

974   Copernicus Atmosphere Monitoring Service (CAMS) report, CAMS84_2018SC3_D5.1.1-2020.pdf,

975   June 2021, doi:10.24380/8gf9-k005.

976   European Space Agency (ESA): The four candidate Earth explorer core missions: Atmospheric

977   dynamics mission, ESA Report for Mission Selection ESA SP, 1233, 145 pp., 1999

978

979 European Space Agency (ESA): ADM-Aeolus Science Report, ESA SP-1311, 121 pp., available at:
980 https://earth.esa.int/documents/10174/1590943/AEOL002.pdf (last access: 14 June 2022), 2008.

981

982 European Space Agency (ESA): "ADM-Aeolus Mission Requirements Document", ESA EOP-
983 SM/2047, 57 pp., available at: http://esamultimedia.esa.int/docs/EarthObservation/ADM-
984 Aeolus_MRD.pdf (last access: 2 November 2019), 2016.

985

986 Fernald, F. G.: Analysis of atmospheric lidar observations: some comments, Appl. Opt., 23, 652–653,
987 doi.org/10.1364/AO.23.000652, 1984.

988

989 Flamant, P., Dabas, A., Martinet, P., Lever, V., Flament, T., Trapon, D., Olivier, M., Cuesta, J., and
990 Huber, D.: Aeolus L2A Algorithm Theoretical Baseline Document, Particle optical properties
991 product, version 5.7, available at: https://earth.esa.int/eogateway/ catalog/aeolus-l2a-aerosol-cloud-
992 optical-product (last access: 14 December 2021), 2021.

993

994 Flament, T., Trapon, D., Lacour, A., Dabas, A., Ehlers, F., and Huber, D.: Aeolus L2A aerosol optical
995 properties product: standard correct algorithm and Mie correct algorithm, Atmos. Meas. Tech., 14,
996 7851–7871, https://doi.org/10.5194/amt-14-7851-2021, 2021.

997

998 Fountoulakis, I., Papachristopoulou, K., Proestakis, E., Gkikas, A., Ioannis Raptis, P., Siomos, N.,
999 Kontoes, C., and Kazadzis, S.: Effect of aerosol vertical distribution on the transfer of solar radiation
1000 through the atmosphere, EGU21-6111, https://doi.org/10.5194/egusphere-egu21-6111, 2021.

1001

1002 Freudenthaler, V.: About the effects of polarising optics on lidar signals and the Δ90 calibration,
1003 Atmos. Meas. Tech., 9, 4181–4255, https://doi.org/10.5194/amt-9-4181-2016, 2016.

1004

1005 Freudenthaler, V., Linné, H., Chaikovski, A., Rabus, D., Groß, S.: EARLINET lidar quality assurance
1006 tools, Atmos. Chem. Phys. Discuss., https://doi.org/10.5194/amt-2017-395, 2018.

1007

1008 Gelaro, R, McCarty, W., Suárez, M. J., Todling, R., Molod, A., Takacs, L., Randles, C. A., Darmenov,
1009 A., Bosilovich, M. G., Reichle, R., Wargan, K., Coy, L., Cullather, R., Draper, C., Akella, S.,
1010 Buchard, V., Conaty, A., da Silva, A. M., Gu, W., Kim, G., Koster, R., Lucchesi, R., Merkova, D.,
1011 Nielsen, J. E., Partyka, G., Pawson, S., Putman, W., Rienecker, M., Schubert, S. D., Sienkiewicz, M.,

1012 and Zhao, B.: The Modern-Era Retrospective Analysis for Research and Applications, Version 2

1013 (MERRA-2), J. Climate, 30, 5419–5454, https://doi.org/10.1175/JCLI-D-16-0758.1, 2017.

1014

1015 Gerasopoulos, E., Andreae, M. O., Zerefos, C. S., Andreae, T. W., Balis, D., Formenti, P., Merlet, P.,

1016 Amiridis, V., and Papastefanou, C.: Climatological aspects of aerosol optical properties in Northern

1017 Greece, Atmos. Chem. Phys., 3, 2025–2041, https://doi.org/10.5194/acp-3-2025-2003, 2003.

1018

1019 Gerasopoulos, E., Amiridis, V., Kazadzis, S., Kokkalis, P., Eleftheratos, K., Andreae, M. O., Andreae,

1020 T. W., El-Askary, H., and Zerefos, C. S.: Three-year ground based measurements of aerosol optical

1021 depth over the Eastern Mediterranean: the urban environment of Athens, Atmos. Chem. Phys., 11,

1022 2145–2159, https://doi.org/10.5194/acp-11-2145-2011, 2011.

1023

1024 Gialitaki, A., Tsekeri, A., Amiridis, V., Ceolato, R., Paulien, L., Kampouri, A., Gkikas, A., Solomos,

1025 S., Marinou, E., Haarig, M., Baars, H., Ansmann, A., Lapyonok, T., Lopatin, A., Dubovik, O., Groß,

1026 S., Wirth, M., Tsichla, M., Tsikoudi, I., and Balis, D.: Is the near-spherical shape the "new black" for

1027 smoke?, Atmos. Chem. Phys., 20, 14005–14021, https://doi.org/10.5194/acp-20-14005-2020, 2020.

1028

1029 Giles, D. M., Sinyuk, A., Sorokin, M. G., Schafer, J. S., Smirnov, A., Slutsker, I., Eck, T. F., Holben,

1030 B. N., Lewis, J. R., Campbell, J. R., Welton, E. J., Korkin, S. V., and Lyapustin, A. I.: Advancements

1031 in the Aerosol Robotic Network (AERONET) Version 3 database – automated near-real-time quality

1032 control algorithm with improved cloud screening for Sun photometer aerosol optical depth (AOD)

1033 measurements, Atmos. Meas. Tech., 12, 169–209, https://doi.org/10.5194/amt-12-169-2019, 2019.

1034

1035 Gkikas, A., Houssos, E. E., Lolis, C. J., Bartzokas, A., Mihalopoulos, N., and Hatzianastassiou, N.:

1036 Atmospheric circulation evolution related to desert-dust episodes over the Mediterranean, Q. J. Roy.

1037 Meteor. Soc., 141, 1634–1645, https://doi.org/10.1002/qj.2466, 2015.

1038

1039 Gkikas, A., Basart, S., Hatzianastassiou, N., Marinou, E., Amiridis, V., Kazadzis, S., Pey, J., Querol,

1040 X., Jorba, O., Gassó, S., and Baldasano, J. M.: Mediterranean intense desert dust outbreaks and their

1041 vertical structure based on remote sensing data, Atmos. Chem. Phys., 16, 8609–8642,

1042 https://doi.org/10.5194/acp-16-8609-2016, 2016.

1043

1044 Gkikas, A., Obiso, V., Pérez García-Pando, C., Jorba, O., Hatzianastassiou, N., Vendrell, L., Basart,

1045 S., Solomos, S., Gassó, S., and Baldasano, J. M.: Direct radiative effects during intense Mediterranean

Atmospheric
Measurement
Techniques
Discussions

Open Access

EGU

desert dust outbreaks, Atmos. Chem. Phys., 18, 8757–8787, https://doi.org/10.5194/acp-18-8757-2018, 2018.

Gkikas, A., Proestakis, E., Amiridis, V., Kazadzis, S., Di Tomaso, E., Marinou, E., Hatzianastassiou, N., Kok, J. F., and García-Pando, C. P.: Quantification of the dust optical depth across spatiotemporal scales with the MIDAS global dataset (2003–2017), Atmos. Chem. Phys., 22, 3553–3578, https://doi.org/10.5194/acp-22-3553-2022, 2022.

Gueymard, C. A. and Yang, D.: Worldwide validation of CAMS and MERRA-2 reanalysis aerosol optical depth products using 15 years of AERONET observations, Atmos. Environ., 225, 117216, https://doi.org/10.1016/j.atmosenv.2019.117216, 2020.

Haywood, J. M., Abel, S. J., Barrett, P. A., Bellouin, N., Blyth, A., Bower, K. N., Brooks, M., Carslaw, K., Che, H., Coe, H., Cotterell, M. I., Crawford, I., Cui, Z., Davies, N., Dingley, B., Field, P., Formenti, P., Gordon, H., de Graaf, M., Herbert, R., Johnson, B., Jones, A. C., Langridge, J. M., Malavelle, F., Partridge, D. G., Peers, F., Redemann, J., Stier, P., Szpek, K., Taylor, J. W., Watson-Parris, D., Wood, R., Wu, H., and Zuidema, P.: The CLoud–Aerosol–Radiation Interaction and Forcing: Year 2017 (CLARIFY-2017) measurement campaign, Atmos. Chem. Phys., 21, 1049–1084, https://doi.org/10.5194/acp-21-1049-2021, 2021.

Health Effects Institute, 2019, State of Global Air 2019, Special Report, Boston, MA: Health Effects Institute, ISSN 2578-6873, https://www.stateofglobalair.org/sites/default/files/soga_2019_report.pdf, 2019.

Horányi, A., Cardinali, C., Rennie, M., and Isaksen, L.: The assimilation of horizontal line-of-sight wind information into the ECMWF data assimilation and forecasting system. Part I: The assessment of wind impact, Q. J. R. Meteorol. Soc., 141, 1223–1232, https://doi.org/10.1002/qj.2430, 2015a.

Horányi, A., Cardinali, C., Rennie, M., and Isaksen, L.: The assimilation of horizontal line-of-sight wind information into the ECMWF data assimilation and forecasting system. Part II: The impact of degraded wind observations, Q. J. R. Meteorol. Soc., 141, 1233–1243, https://doi.org/10.1002/qj.2551, 2015b.

1079 Illingworth, A. J., Barker, H. W., Beljaars, A., Ceccaldi, M., Chepfer, H., Clerbaux, N., Cole, J.,

1080 Delanoë, J., Domenech, C., Donovan, D. P., Fukuda, S., Hirakata, M., Hogan, R. J., Huenerbein, A.,

1081 Kollias, P., Kubota, T., Nakajima, T., Nakajima, T. Y., Nishizawa, T., Ohno, Y., Okamoto, H., Oki,

1082 R., Sato, K., Satoh, M., Shephard, M. W., Velázquez-Blázquez, A., Wandinger, U., Wehr, T., and

1083 van Zadelhoff, G.-J.: The EarthCARE Satellite: The Next Step Forward in Global Measurements of

1084 Clouds, Aerosols, Precipitation, and Radiation, Bull. Amer. Meteor. Soc., 96, 1311–1332,

1085 https://doi.org/10.1175/BAMS-D-12-00227.1, 2015.

1086

1087 Inness, A., Ades, M., Agustí-Panareda, A., Barré, J., Benedictow, A., Blechschmidt, A.-M.,

1088 Dominguez, J. J., Engelen, R., Eskes, H., Flemming, J., Huijnen, V., Jones, L., Kipling, Z., Massart,

1089 S., Parrington, M., Peuch, V.-H., Razinger, M., Remy, S., Schulz, M., and Suttie, M.: The CAMS

1090 reanalysis   of   atmospheric   composition,   Atmos.   Chem.   Phys.,   19,   3515–3556,

1091 https://doi.org/10.5194/acp-19-3515-2019, 2019.

1092

1093 Isaksen, L. and Rennie, M.: A preliminary evaluation of using Aeolus L2B Winds in ECMWF's NWP

1094 system, with focus on the tropical region, in: ESA Living Planet Symposium 2019, Milan, Italy,

1095 https://lps19.esa.int/NikalWebsitePortal/living-planet-symposium-

1096 2019/lps19/Agenda/AgendaItemDetail?id=64570099-bea7-4b8f-a54b-5b6ad81fa342, last access: 8

1097 May 2020, 2019.

1098

1099 Jickells, T. D., An, Z. S., Andersen, K. K., Baker, A. R., Bergametti, G., Brooks, N., Cao, J. J., Boyd,

1100 P. W., Duce, R. A., Hunter, K. A., Kawahata, H., Kubilay, N., laRoche, J., Liss, P. S., Mahowald, N.,

1101 Prospero, J. M., Ridgwell, A. J., Tegen, I. and Torres, R.: Global Iron Connections Between Desert

1102 Dust,   Ocean   Biogeochemistry,   and   Climate,   Science,   308(5718),   67–71,

1103 doi:10.1126/science.1105959, 2005.

1104

1105 Kampouri, A., Amiridis, V., Solomos, S., Gialitaki, A., Marinou, E., Spyrou, C., Georgoulias, A. K.,

1106 Akritidis, D., Papagiannopoulos, N., Mona, L., Scollo, S., Tsichla, M., Tsikoudi, I., Pytharoulis, I.,

1107 Karacostas, T., and Zanis, P.: Investigation of Volcanic Emissions in the Mediterranean: "The Etna–

1108 Antikythera Connection," 12, 40, https://doi.org/10.3390/atmos12010040, 2021.

1109

1110 Kanakidou, M., Mihalopoulos, N., Kindap, T., Im, U., Vrekoussis, M., Gerasopoulos, E., Dermitzaki,

1111 E., Unal, A., Kocak, M., Markakis, K., Melas, D., Kouvarakis, G., Youssef, A. F., Richter, A.,

1112 Hatzianastassiou, N., Hilboll, A., Ebojie, F., Wittrock, F., von Savigny, C., Burrows, J. P.,

1113   Ladstaetter-Weissenmayer, A., and Moubasher, H.: Megacities as hot spots of air pollution in the East

1114   Mediterranean, Atmos. Environ., 45, 1223–1235, https://doi.org/10.1016/j.atmosenv.2010.11.048,

1115   2011.

1116

1117   Kanitz, T., Lochard, J., Marshall, J., McGoldrick, P., Lecrenier, O., Bravetti, P., Reitebuch, O.,

1118   Rennie, M., Wernham, D., and Elfving, A.: Aeolus first light: first glimpse, in: International

1119   Conference on Space Optics – ICSO 2018, 9–12 October 2018, Chania, Greece, vol. 11180, 659–

1120   664, https://doi.org/10.1117/12.2535982, 2019.

1121

1122   Klett, J. D.: Stable analytical inversion solution for processing lidar returns, Appl. Optics, 20, 211–

1123   220, https://doi.org/10.1364/AO.20.000211, 1981.

1124

1125   Kosmopoulos, P. G., Kazadzis, S., El-Askary, H., Taylor, M., Gkikas, A., Proestakis, E., Kontoes, C.

1126   and El-Khayat, M. M.: Earth-Observation-Based Estimation and Forecasting of Particulate Matter

1127   Impact on Solar Energy in Egypt, Remote Sens., 10(12), 1870, doi:10.3390/rs10121870, 2018.

1128

1129   Kosmopoulos, P.G., Kazadzis, S., Taylor, M., Raptis, P.I., Keramitsoglou, I., Kiranoudis, C., and

1130   Bais, A.F.: Assessment of the surface solar irradiance derived from real-time modelling techniques

1131   and verification with ground-based measurements. Atmos. Meas. Tech., 11, pp 907-924, DOI:

1132   10.5194/amt-11-907-2018, 2018.

1133

1134   Lelieveld, J., Berresheim, H., Borrmann, S., Crutzen, P. J., Dentener, F. J., Fischer, H., Feichter, J.,

1135   Flatau, P. J., Heland, J., Holzinger, R., Korrmann, R., Lawrence, M. G., Levin, Z., Markowicz, K.

1136   M., Mihalopoulos, N., Minikin, A., Ramanathan, V., de Reus, M., Roelofs, G. J., Scheeren, H. A.,

1137   Sciare, J., Schlager, H., Schultz, M., Siegmund, P., Steil, B., Stephanou, E. G., Stier, P., Traub, M.,

1138   Warneke, C., Williams, J., and Ziereis, H.: Global Air Pollution Crossroads over the Mediterranean,

1139   Science, 298, 794–799, https://doi.org/10.1126/science.1075457, 2002.

1140

1141   Lelieveld, J., Evans, J. S., Fnais, M., Giannadaki, D., and Pozzer, A.: The contribution of outdoor air

1142   pollution sources to premature mortality on a global scale, Nature, 525, 367–371,

1143   https://doi.org/10.1038/nature15371, 2015.

1144

Atmospheric
Measurement
Techniques
Discussions

1145   Levy, R. C., Mattoo, S., Munchak, L. A., Remer, L. A., Sayer, A. M., Patadia, F., and Hsu, N. C.:

1146   The Collection 6 MODIS aerosol products over land and ocean, Atmos. Meas. Tech., 6, 2989–3034,

1147   https://doi.org/10.5194/amt-6-2989-2013, 2013.

1148

1149   Li, W., El-Askary, H., Qurban, M. A., Proestakis, E., Garay, M. J., Kalashnikova, O. V., Amiridis,

1150   V., Gkikas, A., Marinou, E., Piechota, T., and Manikandan, K. P.: An Assessment of Atmospheric

1151   and Meteorological Factors Regulating Red Sea Phytoplankton Growth, Remote Sens., 10, 673,

1152   https://doi.org/10.3390/rs10050673, 2018.

1153

1154   Li, J., Carlson, B.E., Yung, Y.L. et al. Scattering and absorbing aerosols in the climate system. Nat

1155   Rev Earth Environ 3, 363–379 (2022). https://doi.org/10.1038/s43017-022-00296-7

1156

1157   Liu, D., Wang, Z., Liu, Z., Winker, D., and Trepte, C.: A height resolved global view of dust aerosols

1158   from the first year CALIPSO lidar measurements, J. Geophys. Res.-Atmos., 113, D16214,

1159   https://doi.org/10.1029/2007JD009776, 2008.

1160

1161   Liu, Z., Kar, J., Zeng, S., Tackett, J., Vaughan, M., Avery, M., Pelon, J., Getzewich, B., Lee, K.-P.,

1162   Magill, B., Omar, A., Lucker, P., Trepte, C., and Winker, D.: Discriminating between clouds and

1163   aerosols in the CALIOP version 4.1 data products, Atmos. Meas. Tech., 12, 703–734,

1164   https://doi.org/10.5194/amt-12-703-2019, 2019.

1165

1166   Lux, O., Lemmerz, C., Weiler, F., Marksteiner, U., Witschas, B., Rahm, S., Geiß, A., and Reitebuch,

1167   O.: Intercomparison of wind observations from the European Space Agency's Aeolus satellite mission

1168   and the ALADIN Airborne Demonstrator, Atmos. Meas. Tech., 13, 2075–2097,

1169   https://doi.org/10.5194/amt-13-2075-2020, 2020.

1170

1171   Lux, O., Lemmerz, C., Weiler, F., Marksteiner, U., Witschas, B., Rahm, S., Geiß, A., Schäfler, A.,

1172   and Reitebuch, O.: Retrieval improvements for the ALADIN Airborne Demonstrator in support of

1173   the Aeolus wind product validation, Atmos. Meas. Tech., 15, 1303–1331,

1174   https://doi.org/10.5194/amt-15-1303-2022, 2022.

1175

1176   Mallios, S. A., Daskalopoulou, V., and Amiridis, V.: Orientation of non spherical prolate dust

1177   particles moving vertically in the Earth's atmosphere, J. Aerosol Sci., 151, 105657,

1178   doi:https://doi.org/10.1016/j.jaerosci.2020.105657, 2021.

1179

1180 Marinou, E., Amiridis, V., Binietoglou, I., Tsikerdekis, A., Solomos, S., Proestakis, E., Konsta, D.,

1181 Papagiannopoulos, N., Tsekeri, A., Vlastou, G., Zanis, P., Balis, D., Wandinger, U. and Ansmann,

1182 A.: Three-dimensional evolution of Saharan dust transport towards Europe based on a 9-year

1183 EARLINET-optimized CALIPSO dataset, Atmos. Chem. Phys., 17(9), 5893–5919, doi:10.5194/acp-

1184 17-5893-2017, 2017.

1185

1186 Matthias, V., Freudenthaler, V., Amodeo, A., Balin, I., Balis, D., Bösenberg, J., Chaikovsky, A.,

1187 Chourdakis, G., Comeron, A., Delaval, A., De Tomasi, F., Eixmann, R., Hågård, A., Komguem, L.,

1188 Kreipl, S., Matthey, R., Rizi, V., Rodrigues, J., Wandinger, U., and Wang, X.: Aerosol lidar

1189 intercomparison in the framework of the EARLINET project. 1. Instruments, Appl. Opt., 43, 961-

1190 976, doi:10.1364/AO.43.000961, 2004.

1191

1192 Mattis, I., D'Amico, G., Baars, H., Amodeo, A., Madonna, F., and Iarlori, M.: EARLINET Single

1193 Calculus Chain – technical – Part 2: Calculation of optical products, Atmos. Meas. Tech., 9, 3009–

1194 3029, https://doi.org/10.5194/amt-9-3009-2016, 2016.

1195

1196 McGill, M. J., Yorks, J. E., Scott, V. S., Kupchock, A. W., and Selmer, P. A.: The Cloud Aerosol

1197 Transport System (CATS): A technology demonstration on the International Space Station, Proc.

1198 SPIE 9612, Lidar Remote Sensing for Environmental Monitoring XV, 96120A,

1199 https://doi.org/10.1117/12.2190841, 2015.

1200

1201 MétéoFrance: Algorithm theoretical basis document for cloud products (CMa-PGE01 v3.2, CT-

1202 PGE02 v2.2 & CTTH-PGE03 v2.2), Technical Report SAF/NWC/CDOP/MFL/SCI/ATBD/01,

1203 Paris: MétéoFrance, 2013.

1204

1205 Middleton, N., Tozer, P., and Tozer, B.: Sand and dust storms: underrated natural hazards, Disasters,

1206 43, 390–409, https://doi.org/10.1111/disa.12320, 2018.

1207

1208 Mishchenko, M. I. and Hovenier, J. W.: Depolarization of light backscattered by randomly oriented

1209 nonspherical particles, Opt. Lett., 20(12), 1356, doi:10.1364/OL.20.001356, 1995.

1210

Atmospheric
Measurement
Techniques
Discussions

Open Access

EGU

1211   Müller, D., Ansmann, A., Mattis, I., Tesche, M., Wandinger, U., Althausen, D., & Pisani, G. (2007).

1212   Aerosol-type-dependent lidar ratios observed with raman lidar. Journal of Geophysical Research

1213   Atmospheres, 112(16) doi:10.1029/2006JD008292

1214

1215   Okin, G. S., Mahowald, N., Chadwick, O. A. and Artaxo, P.: Impact of desert dust on the

1216   biogeochemistry of phosphorus in terrestrial ecosystems, Global Biogeochemical Cycles, 18(2),

1217   doi:10.1029/2003GB002145, 2004.

1218

1219   Papagiannopoulos, N., D'Amico, G., Gialitaki, A., Ajtai, N., Alados-Arboledas, L., Amodeo, A.,

1220   Amiridis, V., Baars, H., Balis, D., Binietoglou, I., Comerón, A., Dionisi, D., Falconieri, A., Fréville,

1221   P., Kampouri, A., Mattis, I., Mijić, Z., Molero, F., Papayannis, A., Pappalardo, G., Rodríguez-Gómez,

1222   A., Solomos, S. and Mona, L.: An EARLINET early warning system for atmospheric aerosol aviation

1223   hazards, Atmospheric Chemistry and Physics, 20(18), 10775–10789, doi:https://doi.org/10.5194/acp-

1224   20-10775-2020, 2020.

1225

1226   Pappalardo, G., Amodeo, A., Apituley, A., Comeron, A., Freudenthaler, V., Linné, H., Ansmann, A.,

1227   Bösenberg, J., D'Amico, G., Mattis, I., Mona, L., Wandinger, U., Amiridis, V., Alados-Arboledas,

1228   L., Nicolae, D., and Wiegner, M.: EARLINET: towards an advanced sustainable European aerosol

1229   lidar network, Atmos. Meas. Tech., 7, 2389–2409, https://doi.org/10.5194/amt-7-2389-2014, 2014.

1230

1231   Papayannis, A., Balis, D., Amiridis, V., Chourdakis, G., Tsaknakis, G., Zerefos, C., Castanho, A. D.

1232   A., Nickovic, S., Kazadzis, S., and Grabowski, J.: Measurements of Saharan dust aerosols over the

1233   Eastern Mediterranean using elastic backscatter-Raman lidar, spectrophotometric and satellite

1234   observations in the frame of the EARLINET project, Atmos. Chem. Phys., 5, 2065–2079,

1235   https://doi.org/10.5194/acp-5-2065-2005, 2005.

1236

1237   Paschou, P., Siomos, N., Tsekeri, A., Louridas, A., Georgoussis, G., Freudenthaler, V., Binietoglou,

1238   I., Tsaknakis, G., Tavernarakis, A., Evangelatos, C., von Bismarck, J., Kanitz, T., Meleti, C.,

1239   Marinou, E., and Amiridis, V.: The eVe reference polarisation lidar system for Cal/Val of Aeolus

1240   L2A product, Atmos. Meas. Tech. Discuss. [preprint], https://doi.org/10.5194/amt-2021-268, in

1241   review, 2021.

1242

1243   Pappalardo, G., Wandinger, U., Mona, L., Hiebsch, A., Mattis, I., Amodeo, A., Ansmann, A., Seifert,

1244   P., Linne, H., Apituley, A., Alados Arboledas, L., Balis, D., Chaikovsky, A., D'Amico, G., De

1245 Tomasi, F., Freudenthaler, V., Giannakaki, E., Giunta, A., Grigorov, I., Iarlori, M., Madonna, F.,

1246 Mamouri, R.-E., Nasti, L., Papayannis, A., Pietruczuk, A., Pujadas, M., Rizi, V., Rocadenbosch, F.,

1247 Russo, F., Schnell, F., Spinelli, N., Wang, X., and Wiegner, M.: EARLINET correlative

1248 measurements for CALIPSO: First intercomparison results, J. Geophys. Res., 115, D00H19,

1249 doi:10.1029/2009JD012147, 2010.

1250

1251 Pappalardo, G., Amodeo, A., Apituley, A., Comeron, A., Freudenthaler, V., Linné, H., Ansmann, A.,

1252 Bösenberg, J., D'Amico, G., Mattis, I., Mona, L., Wandinger, U., Amiridis, V., Alados-Arboledas,

1253 L., Nicolae, D., and Wiegner, M.: EARLINET: towards an advanced sustainable European aerosol

1254 lidar network, Atmos. Meas. Tech., 7, 2389–2409, https://doi.org/10.5194/amt-7-2389-2014, 2014.

1255

1256 Pérez, C., Nickovic, S., Pejanovic, G., Baldasano, J. M., and Özsoy, E.: Interactive dust-radiation

1257 modeling: A step to improve weather forecasts, J. Geophys. Res., 111, 1–17, 2006.

1258

1259 Pisso, I., Sollum, E., Grythe, H., Kristiansen, N.I., Cassiani, M., Eckhardt, S., Arnold, D., Morton,

1260 D., Thompson, R.L., Groot Zwaaftink, C.D., Evangeliou, N., Sodemann, H., Haimberger, L., Henne,

1261 S., Brunner, D., Burkhart, J.F., Fouilloux, A., Brioude, J., Philipp, A., Seibert, P., and Stohl, A.:

1262 FLEXPART 10.4 (Version 10.4), Geosci. Model Dev. Discuss. Zenodo,

1263 https://doi.org/10.5281/zenodo.3542278, 2019.

1264

1265 Pöschl, U.: Atmospheric Aerosols: Composition, Transformation, Climate and Health Effects,

1266 ANGEW CHEM INT EDIT, 44, 7520-7540, 10.1002/anie.200501122, 2005.

1267

1268 Proestakis, E., Amiridis, V., Marinou, E., Georgoulias, A. K., Solomos, S., Kazadzis, S., Chimot, J.,

1269 Che, H., Alexandri, G., Binietoglou, I., Daskalopoulou, V., Kourtidis, K. A., de Leeuw, G. and

1270 Ronald, J. van der A.: Nine-year spatial and temporal evolution of desert dust aerosols over South

1271 and East Asia as revealed by CALIOP, Atmos. Chem. Phys., 18(2), 1337–1362, doi:10.5194/acp-18-

1272 1337-2018, 2018.

1273

1274 Proestakis, E., Amiridis, V., Marinou, E., Binietoglou, I., Ansmann, A., Wandinger, U., Hofer, J.,

1275 Yorks, J., Nowottnick, E., Makhmudov, A., Papayannis, A., Pietruczuk, A., Gialitaki, A., Apituley,

1276 A., Szkop, A., Muñoz Porcar, C., Bortoli, D., Dionisi, D., Althausen, D., Mamali, D., Balis, D.,

1277 Nicolae, D., Tetoni, E., Liberti, G. L., Baars, H., Mattis, I., Stachlewska, I. S., Voudouri, K. A., Mona,

1278 L., Mylonaki, M., Perrone, M. R., Costa, M. J., Sicard, M., Papagiannopoulos, N., Siomos, N.,

1279   Burlizzi, P., Pauly, R., Engelmann, R., Abdullaev, S., and Pappalardo, G.: EARLINET evaluation of

1280   the CATS Level 2 aerosol backscatter coefficient product, Atmos. Chem. Phys., 19, 11743–11764,

1281   https://doi.org/10.5194/acp-19-11743-2019, 2019.

1282

1283   Pye, H.O.T., Ward-Caviness, C.K., Murphy, B.N. et al. Secondary organic aerosol association with

1284   cardiorespiratory disease mortality in the United States. Nat Commun 12, 7215 (2021).

1285   https://doi.org/10.1038/s41467-021-27484-1

1286

1287   Randles, C. A., da Silva, A. M., Buchard, V., Colarco, P. R., Darmenov, A., Govindaraju, R.,

1288   Smirnov, A., Holben, B., Ferrare, R., Hair, J., Shinozuka, Y., Flynn, C. J., Randles, C. A., Silva, A.

1289   M. da, Buchard, V., Colarco, P. R., Darmenov, A., Govindaraju, R., Smirnov, A., Holben, B., Ferrare,

1290   R., Hair, J., Shinozuka, Y., and Flynn, C. J.: The MERRA-2 Aerosol Reanalysis, 1980 Onward. Part

1291   I: System Description and Data Assimilation Evaluation, J. Climate, 30, 6823–6850,

1292   https://doi.org/10.1175/JCLI-D-16-0609.1, 2017.

1293

1294   Reitebuch, O., Lemmerz, C., Lux, O., Marksteiner, U., Rahm, S., Weiler, F., Witschas, B., Meringer,

1295   M., Schmidt, K., Huber, D., Nikolaus, I., Geiss, A., Vaughan, M., Dabas, A., Flament, T., Stieglitz,

1296   H., Isaksen, L., Rennie, M., de Kloe, J., Marseille, G.-J., Stoffelen, A., Wernham, D., Kanitz, T.,

1297   Straume, A.-G., Fehr, T., von Bismarck, J., Floberghagen, R., and Par- rinello, T.: Initial Assessment

1298   of the Performance of the First Wind Lidar in Space on Aeolus, EPJ Web Conf., 237, 01010,

1299   https://doi.org/10.1051/epjconf/202023701010, 2020.

1300

1301   Remer, L. A., Kleidman, R. G., Levy, R. C., Kaufman, Y. J., Tanré, D., Mattoo, S., Martins, J. V.,

1302   Ichoku, C., Koren, I., Yu, H. and Holben, B. N.: Global aerosol climatology from the MODIS satellite

1303   sensors, J. Geophys. Res.-Atmos., 113, D14S07, https://doi.org/10.1029/2007JD009661, 2008.

1304

1305   Rennie, M. P. and Isaksen, L.: Investigations Into the Quality of Aeolus L2B Winds Using the

1306   ECMWF Model and Initial NWP Impact Assessment, in: ESA Living Planet Symposium 2019,

1307   Milan,   Italy,   https://lps19.esa.int/NikalWebsitePortal/living-planet-symposium-

1308   2019/lps19/Agenda/AgendaItemDetail?id=1a3d272c-f7d1-4847-b1c4-08c452f9405f, last access: 8

1309   May 2020, 2019.

1310

1311   Rennie, M. P., Isaksen, L., Weiler, F., de Kloe, J., Kanitz, T., and Reitebuch, O.: The impact of Aeolus

1312   wind retrievals on ECMWF global weather forecasts, Q. J. Roy. Meteor. Soc., 147, 3555–3586,

1313   https://doi.org/10.1002/qj.4142, 2021.

1314

1315   Richardson, S. C., Mytilinaios, M., Foskinis, R., Kyrou, C., Papayannis, A., Pyrri, I., Giannoutsou,

1316   E., and Adamakis, I. D. S.: Bioaerosol detection over Athens, Greece using the laser induced

1317   fluorescence   technique,   Sci.   Total   Environ.,   696,   133906,

1318   https://doi.org/10.1016/j.scitotenv.2019.133906, 2019.

1319

1320   Roebeling, R. A., Feijt, A. J., and Stamnes, P.: Cloud property retrievals for climate monitoring:

1321   implications of differences between SEVIRI on METEOSAT-8 and AVHRR on NOAA-17, J.

1322   Geophys. Res., 111, 20210,   https://doi.org/10.1029/2005JD006990, 2006.

1323

1324   Roy, G. and Roy, N.: Relation between circular and linear depolarization ratios under multiple-

1325   scattering conditions, Appl. Opt., doi:10.1364/ao.47.006563, 2008.

1326

1327   Sasano, Y. and Nakane, H.: Significance of the extinction/backscatter ratio and the boundary value

1328   term in the solution for the two-component lidar equation, Appl. Opt., 23(1), 11_1--13,

1329   doi:10.1364/AO.23.0011_1, 1984.

1330

1331   Sayer, A. M., Hsu, N. C., Bettenhausen, C., and Jeong, M.-J.: Validation and uncertainty estimates

1332   for MODIS Collection 6 "Deep Blue" aerosol data, J. Geophys. Res., 118, 7864–7873,

1333   https://doi.org/10.1002/jgrd.50600, 2013.

1334

1335   Schmetz, J., Pili, P., Tjemkes, S., Just, D., Kerkmann, J., Rota, S., and Ratier, A.: An introduction to

1336   Meteosat   Second   Generation   (MSG),   B.   Am.   Meteorol.   Soc.,   83,   977–992,

1337   https://doi.org/10.1175/1520-0477(2002)083<0977:AITMSG>2.3.CO;2, 2002.

1338

1339   Sinyuk, A., Holben, B. N., Eck, T. F., Giles, D. M., Slutsker, I., Korkin, S., Schafer, J. S., Smirnov,

1340   A., Sorokin, M., and Lyapustin, A.: The AERONET Version 3 aerosol retrieval algorithm, associated

1341   uncertainties   and   comparisons   to   Version   2,   Atmos.   Meas.   Tech.,   13,   3375–3411,

1342   https://doi.org/10.5194/amt-13-3375-2020, 2020.

1343

1344 Siomos, N., Balis, D. S., Voudouri, K. A., Giannakaki, E., Filioglou, M., Amiridis, V., Papayannis,
1345 A., and Fragkos, K.: Are EARLINET and AERONET climatologies consistent? The case of
1346 Thessaloniki, Greece, Atmos. Chem. Phys., 18, 11885–11903, https://doi.org/10.5194/acp-18-11885-
1347 2018, 2018.

1349 Solomon S., Dube K., Stone K., Yu P., Kinnison D., Toon O.B., Strahan S.E., Rosenlof K.H.,
1350 Portmann R., Davis S., Randel W., Bernath P., Boone C., Bardeen C.G., Bourassa A., Zawada D.,
1351 Degenstein D.: On the stratospheric chemistry of midlatitude wildfire smoke (2022) Proceedings of
1352 the National Academy of Sciences of the United States of America, 119 (10), pp. e2117325119 DOI:
1353 10.1073/pnas.2117325119

1355 Stoffelen, A., Pailleux, J., Källén, E., Vaughan, J. M., Isaksen, L., Flamant, P., Wergen, W.,
1356 Andersson, E., Schyberg, H., Culoma, A., Meynart, R., Endemann, M., and Ingmann, P.: The
1357 atmospheric dynamics mission for global wind field measurement, B. Am. Meteorol. Soc., 86, 73-87,
1358 https://doi.org/10.1175/BAMS-86-1-73, 2005.

1360 Stohl, A., Forster, C., Frank, A., Seibert, P., and Wotawa, G.: Technical note: The Lagrangian particle
1361 dispersion model FLEXPART version 6.2, Atmos. Chem. Phys., 5, 2461–2474, doi:10.5194/acp-5-
1362 2461-2005, 2005.

1364 Straume, A.G., Schuettemeyer, D., von Bismarck, J., Kanitz, T., Fehr, T., EOP-SM/2945/AGS-ags,
1365 PL-Plan, European Space Agency (ESA),
1366 https://earth.esa.int/eogateway/documents/20142/1564626/Aeolus-Scientific-CAL-VAL-
1367 Implementation-Plan.pdf, 2019.

1369 Straume, A. G., Rennie, M., Isaksen, L., de Kloe, J., Marseille, G.-J., Stoffelen, A., Flament, T.,
1370 Stieglitz, H., Dabas, A., Huber, D., Reitebuch, O., Lemmerz, C., Lux, O., Marksteiner, U., Weiler,
1371 F., Witschas, B., Meringer, M., Schmidt, K., Nikolaus, I., Geiß, A., Flamant, P., Kanitz, T., Wernham,
1372 D., von Bismarck, J., Bley, S., Fehr, T., Floberghagen, R., and Parrinello, T.: ESA's space-based
1373 Doppler wind lidar mission Aeolus – First wind and aerosol product assessment results, EPJ Web
1374 Conf., 237, 01007, https://doi.org/10.1051/epjconf/202023701007, 2020.

1376 Tyrlis, E. and Lelieveld, J.: Climatology and Dynamics of the Summer Etesian Winds over the
1377 Eastern Mediterranean, J. Atmos. Sci., 70, 3374–3396, 2013.

1378

1379 van der Werf, G. R., Randerson, J. T., Giglio, L., van Leeuwen, T. T., Chen, Y., Rogers, B. M., Mu,
1380 M., van Marle, M. J. E., Morton, D. C., Collatz, G. J., Yokelson, R. J., and Kasibhatla, P. S.: Global
1381 fire emissions estimates during 1997–2016, Earth Syst. Sci. Data, 9, 697–720,
1382 https://doi.org/10.5194/essd-9-697-2017, 2017.

1383

1384 Ulanowski, Z., Bailey, J., Lucas, P. W., Hough, J. H., and Hirst, E.: Alignment of atmospheric mineral
1385 dust due to electric field, Atmos. Chem. Phys., 7, 6161–6173, https://doi.org/10.5194/acp-7-6161-
1386 2007, 2007.

1387

1388 Varlas, G.; Marinou, E.; Gialitaki, A.; Siomos, N.; Tsarpalis, K.; Kalivitis, N.; Solomos, S.; Tsekeri,
1389 A.; Spyrou, C.; Tsichla, M.; Kampouri, A.; Vervatis, V.; Giannakaki, E.; Amiridis, V.; Mihalopoulos,
1390 N.; Papadopoulos, A.; Katsafados, P. Assessing Sea-State Effects on Sea-Salt Aerosol Modeling in
1391 the Lower Atmosphere Using Lidar and In-Situ Measurements. Remote Sens., 13, 614.
1392 https://doi.org/10.3390/rs13040614, 2021.

1393

1394 Voudouri, K.A., Siomos, N., Michailidis, K., D'Amico, G., Mattis, I., Balis, D.: Consistency of the
1395 Single Calculus Chain optical products with archived measurements from an EARLINET lidar
1396 station, Remote Sensing. 2020; 12(23):3969. https://doi.org/10.3390/rs12233969, 2020.

1397

1398 Wei, J., Li, Z., Peng, Y., and Sun, L.: MODIS Collection 6.1 aerosol optical depth products over land
1399 and ocean: validation and comparison, Atmos. Environ., 201, 428–440, 2019

1400

1401 Weiler, F., Rennie, M., Kanitz, T., Isaksen, L., Checa, E., de Kloe, J., Okunde, N., and Reitebuch, O.:
1402 Correction of wind bias for the lidar on board Aeolus using telescope temperatures, At- mos. Meas.
1403 Tech., 14, 7167–7185, https://doi.org/10.5194/amt- 14-7167-2021, 2021.

1404

1405 Weinzierl, B., Ansmann, A., Prospero, J. M., Althausen, D., Benker, N., Chouza, F., Dollner, M.,
1406 Farrell, D., Fomba, W. K., Freudenthaler, V., Gasteiger, J., Groß, S., Haarig, M., Heinold, B.,
1407 Kandler, K., Kristensen, T. B., Mayol-Bracero, O. L., Müller, T., Reitebuch, O., Sauer, D., Schäfler,
1408 A., Schepanski, K., Spanu, A., Tegen, I., Toledano, C. and Walser, A.: The Saharan Aerosol Long-
1409 Range Transport and Aerosol–Cloud-Interaction Experiment: Overview and Selected Highlights,
1410 Bull. Amer. Meteor. Soc., 98(7), 1427–1451, doi:10.1175/BAMS-D-15-00142.1, 2016.

1411

1412 Winker, D. M., Vaughan, M. A., Omar, A., Hu, Y., Powell, K. A., Liu, Z., Hunt, W. H. and Young,

1413 S. A.: Overview of the CALIPSO Mission and CALIOP Data Processing Algorithms, J. Atmos.

1414 Ocean. Technol., 26(11), 2310–2323, doi:10.1175/2009JTECHA1281.1, 2009.

1415

1416 Witschas, B., Lemmerz, C., Geiß, A., Lux, O., Marksteiner, U., Rahm, S., Reitebuch, O., and Weiler,

1417 F.: First validation of Aeolus wind observations by airborne Doppler wind lidar measurements,

1418 Atmos. Meas. Tech., 13, 2381–2396, https://doi.org/10.5194/amt-13-2381-2020, 2020.

1419

1420 Witschas, B., Lemmerz, C., Lux, O., Marksteiner, U., Reitebuch, O., Weiler, F., Fabre, F., Dabas, A.,

1421 Flament, T., Huber, D., and Vaughan, M.: Spectral performance analysis of the Aeolus Fabry–Pérot

1422 and Fizeau interferometers during the first years of operation, Atmos. Meas. Tech., 15, 1465–1489,

1423 https://doi.org/10.5194/amt-15-1465-2022, 2022.

1424

1425 Zeng, S., Vaughan, M., Liu, Z., Trepte, C., Kar, J., Omar, A., Winker, D., Lucker, P., Hu, Y.,

1426 Getzewich, B., and Avery, M.: Application of high-dimensional fuzzy k-means cluster analysis to

1427 CALIOP/CALIPSO version 4.1 cloud–aerosol discrimination, Atmos. Meas. Tech., 12, 2261–2285,

1428 https://doi.org/10.5194/amt-12-2261-2019, 2019.

1429

1430 Zerefos, C., Nastos, P., Balis, D., Papayannis, A., Kelepertsis, A., Kannelopoulou, E., Nikolakis, D.,

1431 Eleftheratos, C., Thomas, W., and Varotsos, C.: A complex study of Etna's volcanic plume from

1432 ground-based, in situ and space-borne observations, International J. Remote Sens., 27, 1855–1864,

1433 https://doi.org/10.1080/01431160500462154, 2006.

1434
1435
1436
1437
1438
1439
1440
1441
1442
1443
1444
1445
1446
1447

Atmospheric
Measurement
Techniques
Discussions

1448 **Table 1:** Statistical metrics for the unfiltered (clouds plus aerosols) Aeolus L2A SCA and SCA mid-bin backscatter

1449 profiles at each PANACEA site.

Station	SCA					SCA_mid_bin				
	Counts	Bias	Rel. Bias (%)	R	RMSE	Counts	Bias	Rel. Bias (%)	R	RMSE
ANT	255	0.06	13.63	0.49	1.14	173	0.25	45.59	0.57	1.01
ATH	60	0.73	199.65	0.49	2.26	43	1.16	272.84	0.52	3.10
THE	222	0.83	185.16	0.34	2.60	140	1.10	224.65	0.32	2.19

1450

1451 **Table 2:** As in Table 1 but for the filtered (only aerosols) Aeolus backscatter retrievals.

Station	SCA					SCA_mid_bin				
	Counts	Bias	Rel. Bias (%)	R	RMSE	Counts	Bias	Rel. Bias (%)	R	RMSE
ANT	94	-0.10	-26.57	0.55	0.78	57	0.06	13.35	0.86	0.43
ATH	12	1.08	483.36	0.75	3.33	9	0.73	312.67	0.82	1.41
THE	133	0.46	130.49	0.39	1.86	81	0.55	145.08	0.43	1.20

1452

1453

1454

1455

1456

1457

1458

1459

Atmospheric
Measurement
Techniques
Discussions
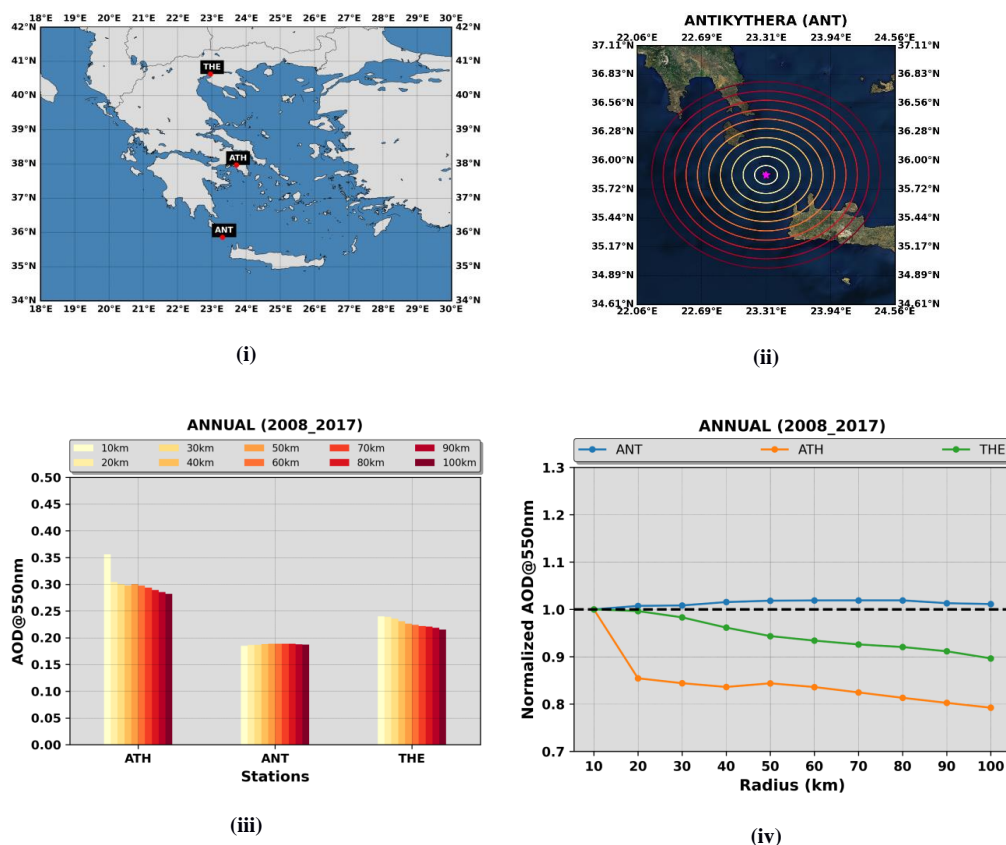
Figure 1: (i) Locations of the three Greek PANACEA sites, namely Athens (ATH), Antikythera (ANT) and Thessaloniki (THE), (ii) Concentric circles, around the Antikythera island, of radii from 10 to 100 km with an incremental step of 10 km, (iii) Climatological MODIS-Aqua AOD levels, representative for the period 2008 – 2017, for each circle area centered at each PANACEA site, (iv) Normalized climatological AODs for each circle area with respect to the corresponding levels of the inner circle.
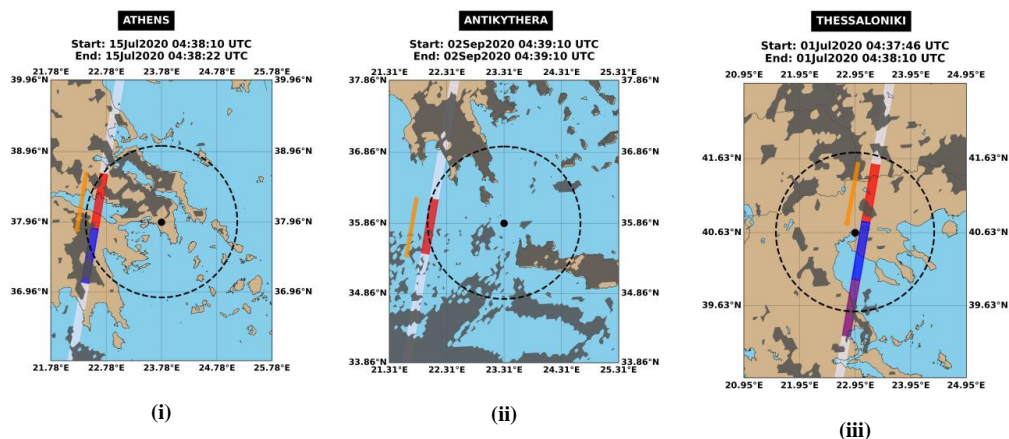
Figure 2: The white stripe indicates the ALADIN's measurements track and the colored rectangles correspond to the Aeolus observations (~90 km along-track averaged measurements) falling within a radius of 120 km (dashed black line) of the PANACEA stations (black dot). The orange arrow shows the Aeolus flight directions (ascending or descending orbit). Dark grey shaded areas: MSG-SEVIRI cloud mask product (CLM) at the nearest time to Aeolus overpass. The start and end time (in UTC) of the ALADIN observations are given in the title of each plot.
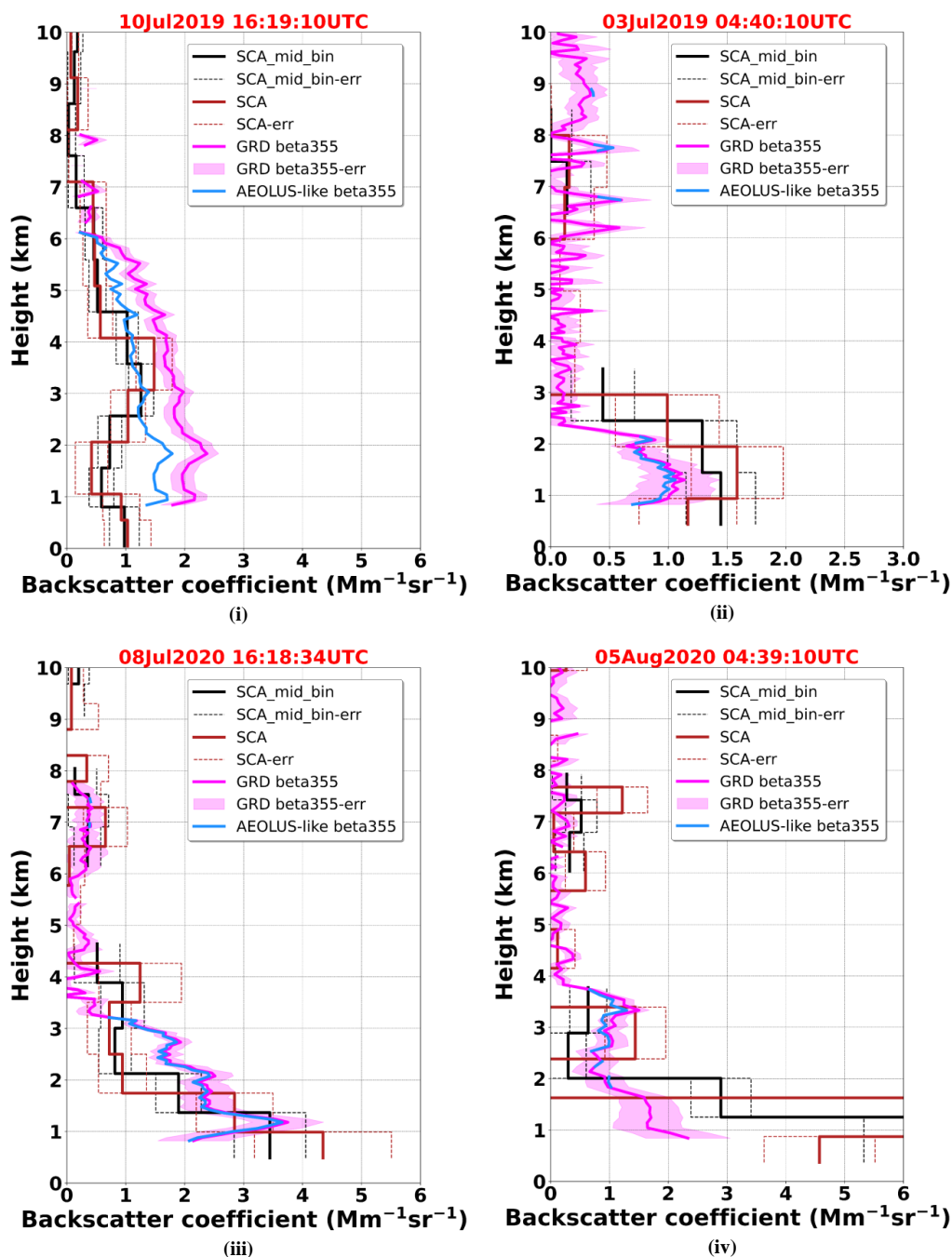
46

Figure 3: Vertical profiles of backscatter coefficient at 355 nm acquired by ALADIN for the Level 2A SCA (regular vertical observation grid, brown solid curve) and SCA mid-bin (reduced vertical observation grid, black solid curve) products. The dashed lines correspond to the estimated SCA backscatter coefficient errors (brown) and SCA mid-bin backscatter coefficient errors (black). Vertical profile of Polly^{XT} backscatter coefficient (pink solid curve) at UV wavelength (355 nm) and associated errors (pink shaded area). Polly^{XT} Aeolus-like backscatter coefficient (light-blue

1501   solid curve) after converting the linear-derived products to circular co-polar according to Paschou et al. (2021). The
1502   ground-based profiles have been acquired at the Antikythera station (southwest Greece) on: (i) 10th July 2019, (ii) 3rd July
1503   2019, (iii) 8th July 2020 and (iv) 5th August 2020. The red color font denotes which Aeolus BRC (along with the overpass
1504   time) has been selected based on the defined collocation criteria.
1505
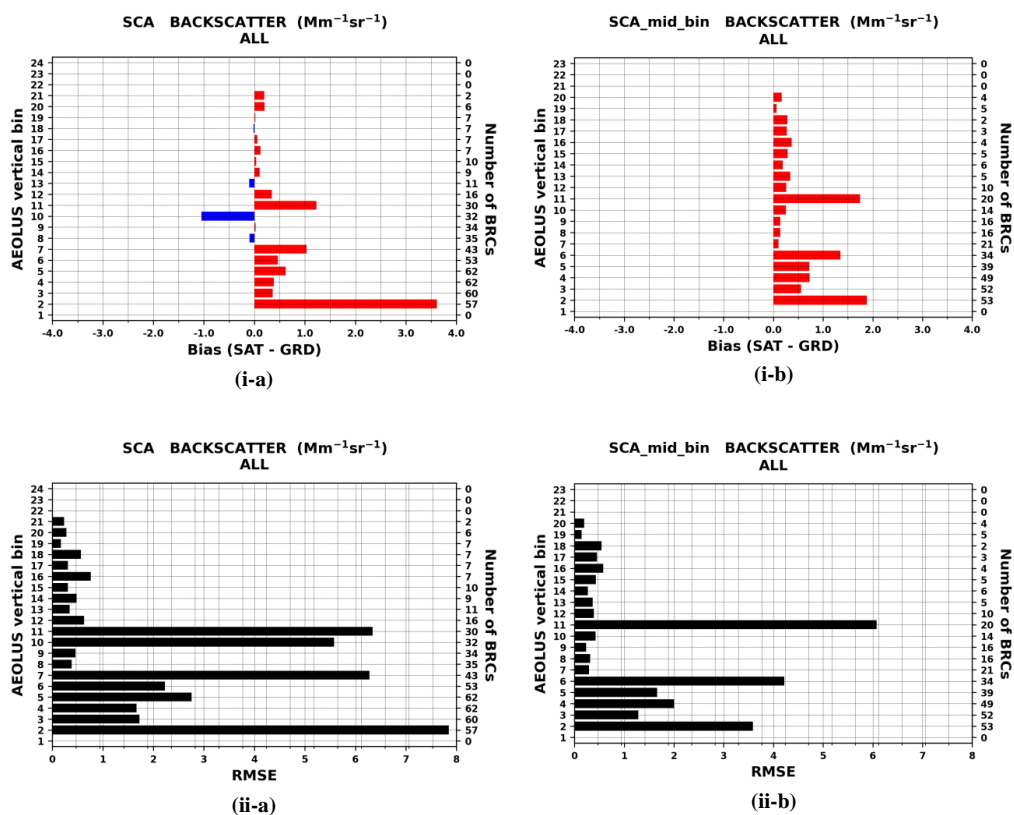
1506   **Figure 4:** Bias (i) and root mean square error (ii) metrics for the unfiltered Aeolus L2A backscatter retrievals reported at
1507   the regular (a) and mid-bin (b) vertical scales. The biases are defined as SAT-GRD and the positive/negative departures
1508   are depicted with red/blue bars. The statistical metrics are vertically resolved based on Aeolus bins indices (left y-axis).
1509   The number of BRCs participating in the metrics calculations at each bin are given on the right y-axis.
1510
1511
1512
1513
1514
1515
1516
1517
1518
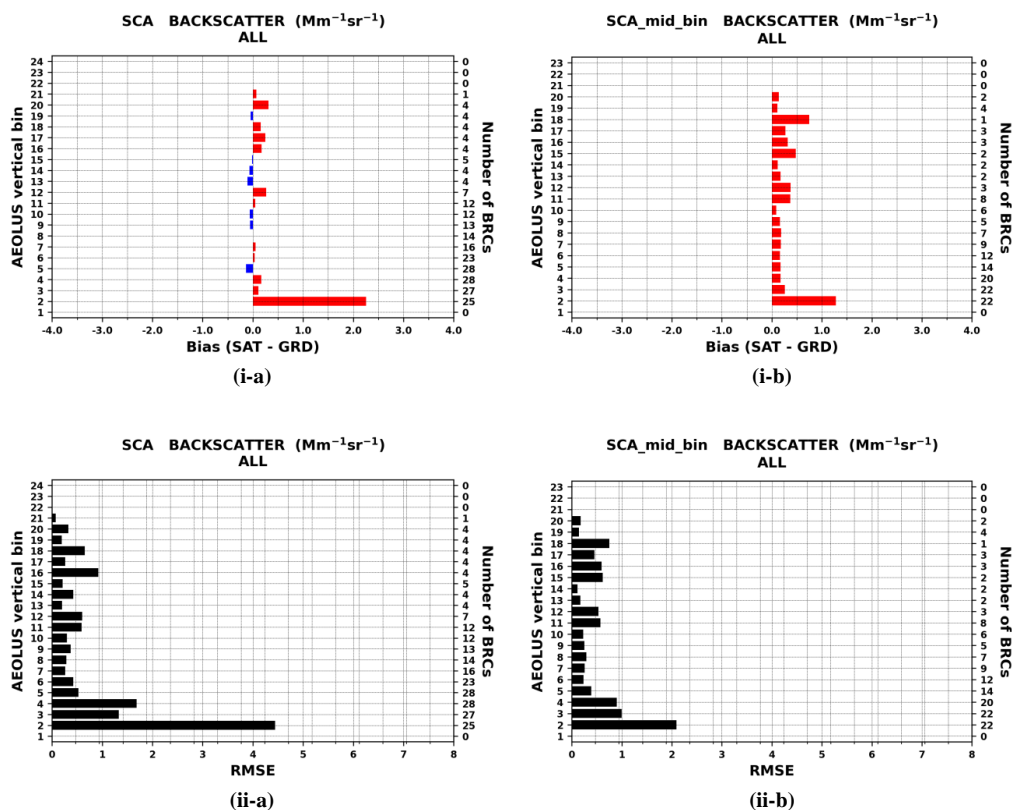
Figure 5: As in Figure 4 but for the filtered Aeolus L2A backscatter retrievals.
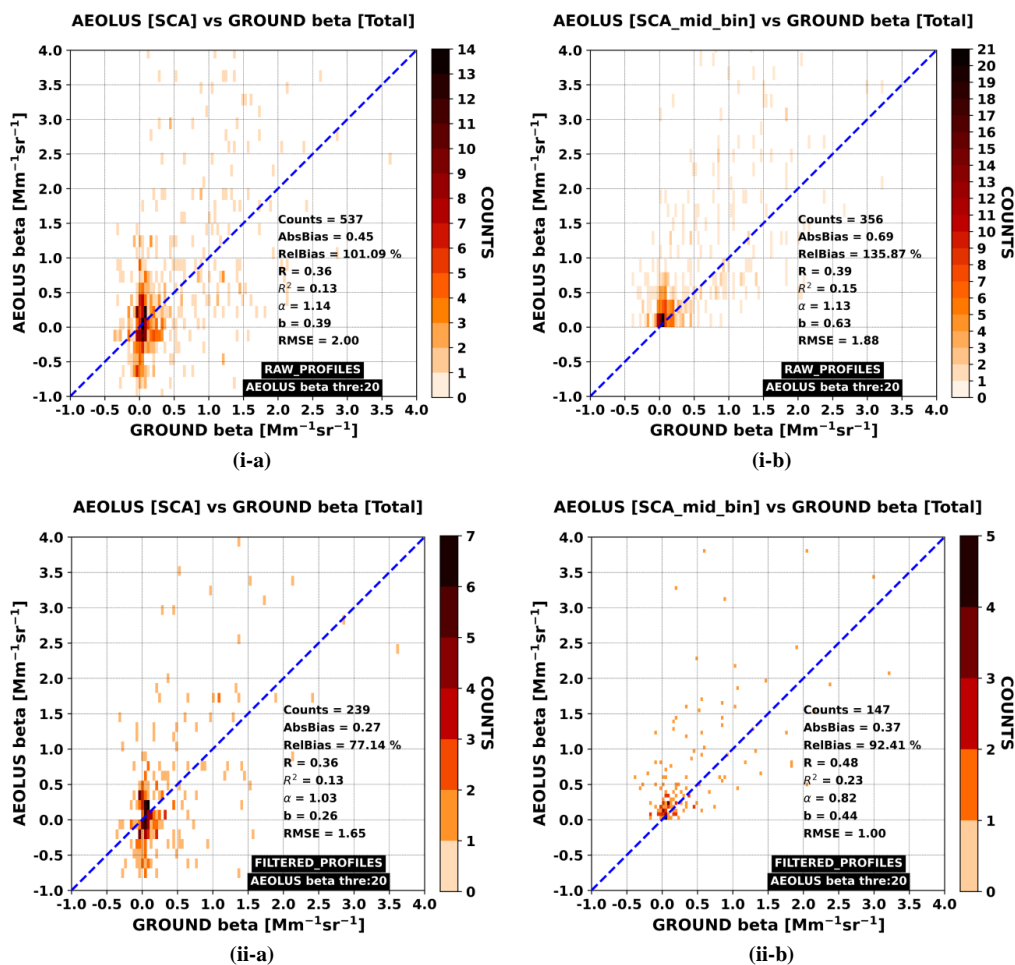
Figure 6: 2D histograms between Aeolus (y-axis) and ground-based (x-axis) backscatter coefficient retrievals. In the upper (i) and bottom (ii) panels are depicted the results for the cloud+aerosol backscatter (unfiltered) and cloud-cleared backscatter (filtered) Aeolus profiles, respectively. On the left and right columns are illustrated the results corresponding to Aeolus regular (24 bins) and mid-bin (23 bins) vertical scales, respectively. Aeolus backscatter values larger than 20 Mm^{-1} sr^{-1} are masked out from the collocated sample.
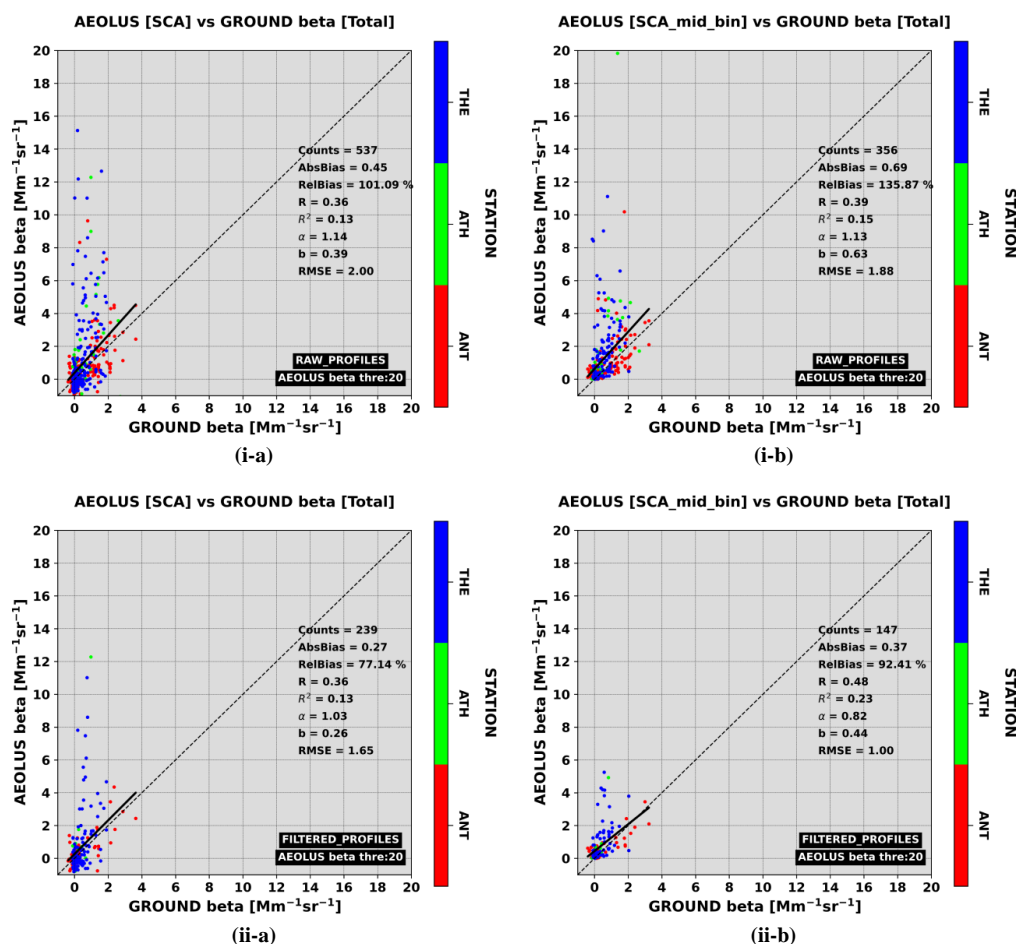
Figure 7: Scatterplots between Aeolus (y-axis) and ground-based (x-axis) backscatter coefficient retrievals resolved based on the indices of Aeolus vertical bins (colored circles). In the upper (i) and bottom (ii) panels are depicted the results for the unfiltered and filtered Aeolus profiles, respectively. On the left and right columns are illustrated the results corresponding to Aeolus regular (24 bins) and mid-bin (23 bins) vertical scales, respectively. Aeolus backscatter values larger than 20 Mm^{-1} sr^{-1} are masked out from the collocated sample.